Advanced Optical Materials

ADVANCED OPTICAL MATERIALS
www.advopticalmat.de

RESEARCH ARTICLE OPEN ACCESS

Naphthyridine-Based Donor–Acceptor Boron Difluoride Complexes Targeting Red Emission in Organic Light-Emitting Diodes

Omar Lahna[1] | Stepan Kutsiy[1,2] | Dmytro Volyniuk[3] | Roman Luboradzki[4] | Elina Andresen[5] | Ute Resch-Genger[5] | Juozas V. Grazulevicius[3] | Pavlo Stakhira[2] | Mykhaylo A. Potopnyk[1,6]

[1]Institute of Organic Chemistry, Polish Academy of Sciences, Warsaw, Poland | [2]Department of Electronic Engineering, Lviv Polytechnic National University, Lviv, Ukraine | [3]Department of Polymer Chemistry and Technology, Kaunas University of Technology, Kaunas, Lithuania | [4]Institute of Physical Chemistry, Polish Academy of Sciences, Warsaw, Poland | [5]Division Biophotonics, Department 1, Bundesanstalt für Materilaforschung und -prüfung (BAM), Berlin, Germany | [6]Department of Organic Chemistry, Faculty of Chemistry, Ivan Franko National University of Lviv, Lviv, Ukraine

Correspondence: Ute Resch-Genger (ute.resch@bam.de) | Juozas V. Grazulevicius (juozas.grazulevicius@ktu.lt) | Pavlo Stakhira (pavlo.y.stakhira@lpnu.ua) | Mykhaylo A. Potopnyk (mykhaylo.potopnyk@icho.edu.pl)

Received: 9 February 2026 | **Revised:** 27 April 2026 | **Accepted:** 21 May 2026

Keywords: difluoroboron dyes | exciplex | optoelectronics | organic semiconductors | solid-state emission | donor-acceptor dyes

ABSTRACT

Four donor–acceptor boron difluoride complexes **1–4** based on triphenylamine electron donor and [1,3,5,2]oxadiazaborinino[3,4-*a*][1,8]naphthyridine acceptor are synthesized and systematically investigated as emissive and charge-transport materials for organic optoelectronics. Comprehensive spectroscopic and electrochemical studies reveal a pronounced intramolecular charge transfer character of these compounds, leading to solvent-polarity-dependent photophysical properties such as bathochromically shifted emission spectra. Charge-carrier mobility measurements demonstrate balanced hole and electron transport properties, highlighting the potential of these materials for optoelectronic applications. In the solid state, compounds **1** and **2** exhibit near-unity photoluminescence quantum yields (PLQY) in polymethylmethacrylate and 1,3-bis(*N*-carbazolyl)benzene matrices, whereas the CF_3-substituted analogues **3** and **4** show markedly red-shifted emission accompanied by reduced PLQYs. The dyes are successfully employed as emitters in organic light-emitting diodes (OLEDs) using doping-free, host-containing, and interface exciplex-forming architectures, as well as multiple ultrathin emissive layer configurations, exhibiting an external quantum efficiency of up to 12.76% in the best case. Furthermore, compounds **3** and **4** enable the fabrication of far-red OLEDs with triple ultrathin emissive layer configurations, exhibiting electroluminescence maxima at 650 and 688 nm, respectively. These results establish donor–acceptor boron difluoride complexes as promising platforms for color-tunable emission and diverse OLED device architectures.

1 | Introduction

Organic light-emitting diodes (OLEDs) have experienced rapid and continuous advancements in response to the growing demand for high-efficiency displays, wide color gamut reproduction, and energy-efficient solid-state lighting [1]. Despite this progress, the realization of efficient red OLEDs remains a significant challenge. Emission in the long-wavelength region

This manuscript is dedicated to the memory of Professor Yaroslav Kalychak (1947–2026).

is often accompanied by an enhanced nonradiative decay due to increased vibrational relaxation and intrinsic efficiency losses associated with the energy-gap law [2–5]. These factors collectively limit the radiative recombination efficiency and device stability. This highlights the need for novel molecular emitters that combine rigid molecular frameworks, precisely controlled electronic structures, and minimized vibrational dissipation, while maintaining compatibility with advanced device architectures.

Boron-centered luminophores, particularly boron difluoride (BF_2) complexes, have emerged as a promising class of materials to address these challenges [6, 7]. Boron difluoride complexes are coordination compounds in which a BF_2 moiety is chelated by organic ligands, most commonly β-diketones or related π-conjugated systems, leading to rigid, planar, and highly stable molecular architectures [8]. The electron-deficient boron center, together with enhanced ligand conjugation, endows these complexes with precisely tunable optical properties, strong fluorescence, and high photostability. As a result, BF_2-based luminophores have been widely explored in diverse applications such as fluorescent probes [9, 10], chemical and biological sensing [11, 12], laser materials [13–15], bioimaging [16, 17], and organic optoelectronic devices [18–21]. Their pronounced sensitivity to local environments, including polarity, pH, and ion coordination, further expands their functional versatility across materials science and analytical chemistry [22–24].

From a photophysical perspective, the strong Lewis acidity of the boron center and its ability to form rigid chelated structures enable an effective modulation of frontier molecular orbitals, suppression of nonradiative decay pathways, and the generation of narrowband emission. In parallel, donor–acceptor (D–A) molecular motifs based on heteroaromatic cores offer additional advantages, including controlled intramolecular charge transfer (ICT), enhanced thermal stability, and broad tunability through molecular engineering [25, 26]. In this context, combining naphthyridine-based frameworks with BF_2 coordination represents an attractive strategy for constructing long-wavelength emitters that combine strong ICT character with structural rigidity, thereby overcoming the efficiency limitations typically associated with orange and red emission [27].

Recently, we developed a new class of *N,O*-coordinated naphthyridine-based, carbazolyl-containing donor–acceptor BF_2 complexes with solid-state luminescence properties tune able by fluorine atoms (Figure 1a) [27]. They demonstrated efficient emission, reaching a photoluminescence quantum yield (PLQY) of 86% in a polymeric matrix due to the aggregation /crystallization-induced emission phenomenon. However, information on the charge-injecting, charge-transporting, and electroluminescent properties of BF_2 complexes remains very limited.

In this work, we present a new family of naphthyridine-based donor–acceptor boron difluoride complexes developed as efficient emitters (Figure 1b) for OLEDs spanning the green to red spectral region. Through rational molecular design, comprehensive structural characterization, and detailed photophysical investigations, we demonstrate how BF_2 coordination enhances molecular rigidity, modulates charge-transfer behavior, and promotes high-yield emission. Two of the compounds exhibit PLQY of 100% in the solid state. The naphthyridine-based donor–acceptor boron difluoride complexes also exhibit bipolar transport properties, with comparable hole and electron mobilities across a wide range of electric fields. When incorporated into optimized OLED architectures, these emitters enable the fabrication of devices with high external quantum efficiencies (EQEs) up to 12.76% and reduced efficiency roll-off. Collectively, these results highlight the effectiveness of a molecular–device co-design strategy and establish naphthyridine–BF_2 complexes as a versatile and promising platform for bipolar light-emitting OLED materials, although their maximum EQEs remain lower than the record values reported elsewhere [28–30].

2 | Results and Discussion

2.1 | Synthesis and Characterization

For the synthesis of compounds **1–4** (Scheme 1), 5,7-dimethyl-1,8-naphthyridin-2-amine (**5**) and 5,7-bis(trifluoro methyl)-1,8-naphthyridin-2-amine (**6**) were used as starting building blocks. First, 4-bromobenzoic acid (**7**) was converted into 4-bromobenzoyl chloride (**10**) by treatment with thionyl chloride in hot toluene. Analogously, 5-bromothiophene-2-carboxylic acid (**9**), synthesized by bromination of thiophene-2-carboxylic acid (**8**), was converted into 5-bromothiophene-2-carbonyl chloride (**11**). Subsequent acylation of amines **5** and **6** with compounds **10** and **11** afforded amides **12–15** in yields of 64–82%. These bromo-derivatives were then subjected to a Suzuki–Miyaura cross-coupling reaction with (4-(diphenylamino)phenyl)boronic acid (**16**) to give products **17–20** in good (91% and 89% for **17** and **18**, respectively) or moderate (54% and 51% for the CF_3 analogues **19** and **20**, respectively) yields. Finally, ligands **17–20** were treated with boron trifluoride under basic conditions to afford the boron difluoride complexes **1–4** in yields of 67–73%.

2.2 | Crystal Structure Analysis

Additionally, the structures of compounds **1**, **2**, and **4** were confirmed by single-crystal X-ray diffraction analysis (Figures S1–S6). In both cases, the oxadiazaborinino-naphthyridinyl core adopts an almost coplanar arrangement with the adjacent phenylene linker in dye **1** or the thiophene linker in dye **2**, with corresponding torsion angles (N3–C11–C12–C13/N3A–C11A–C12A–C13A for compound **1** and N3–C11–C12–S1 for **2**) in the range of 1.8–4.0° (Figure 2a and Figure S5a). In the structure of compound **1**, the torsion angle between the two covalently connected phenylene units (C14–C15–C18–C19/C14A–C15A–C18A–C19A) is 22.5–36.5°. Meanwhile, the analogous angle between the phenylene and thiophene units (C14–C15–C16–C17) in compound **2** is significantly smaller (21.3°). This reduced torsion angle indicates more effective π-conjugation between the triphenylamine and the oxadiazaborinino-naphthyridinyl units in the thiophene-linked compound **2** compared to compound **1**. Therefore, the structural data demonstrate that thiophene acts as a slightly more effective conjugated linker than phenylene in this molecular system.

Boron difluoride complexes **1** and **4** crystallize in the triclinic crystal system with space group *P*-1 [a = 10.59395(19) Å,

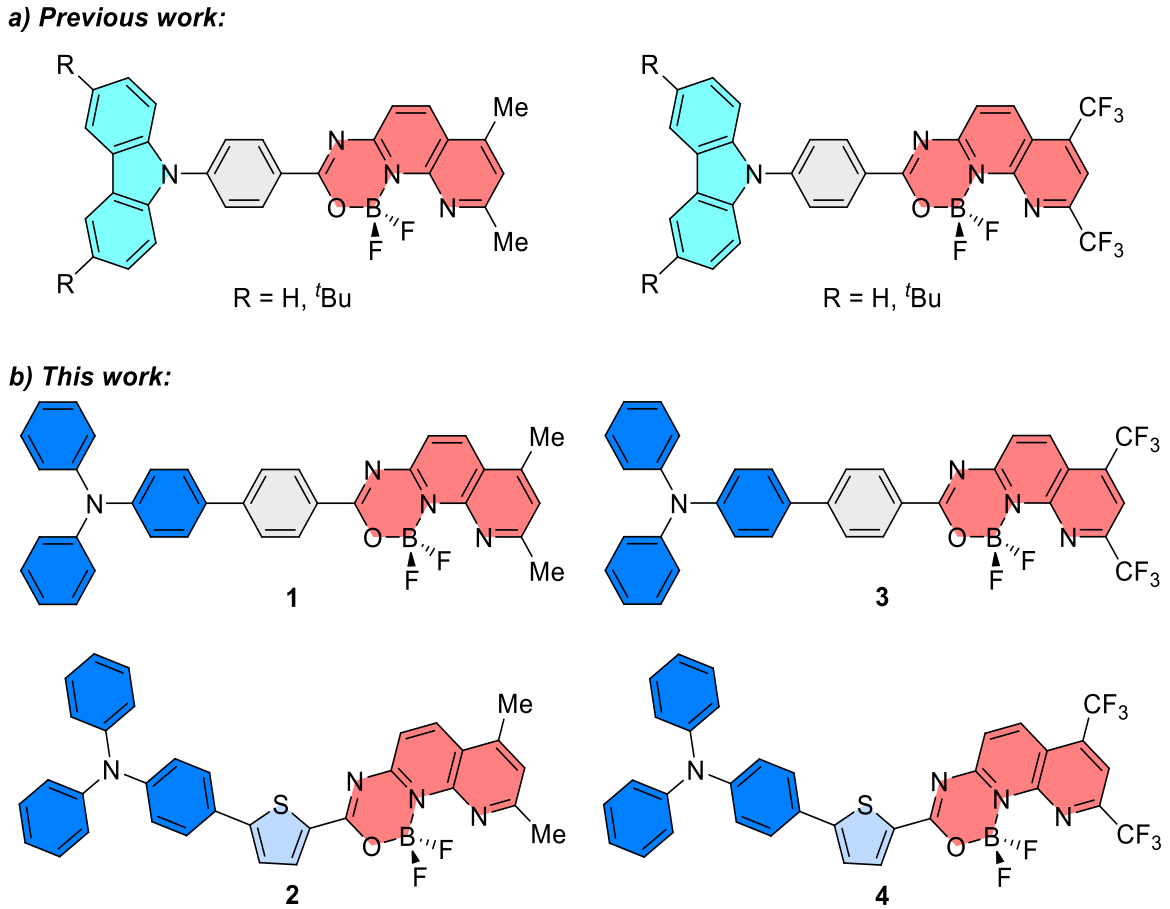

FIGURE 1 | (a) Recently elaborated carbazole-containing dyes. (b) Donor-acceptor triphenylamine-containing boron difluoride complexes **1–4**.

b = 15.2220(3) Å, c = 21.1578(5) Å, α = 109.054(2)°, β = 102.4406(18)°, γ = 90.1192(15)° for compound **1**; and a = 11.0324(3) Å, b = 15.4278(4) Å, c = 18.2429(5) Å, α = 84.003(2)°, β = 75.177(2)°, γ = 86.165(2)° for compound **4**], containing four dye molecules (due to the presence of two symmetrically independent conformers) and two toluene molecules in the unit cell (Tables S1 and S3, and Figures S4 and S6). The thiophene-linked analogue **2** crystallizes in the orthorhombic crystal system with space group *Pbca* [a = 10.42048(5) Å, b = 15.50365(7) Å, c = 33.44011(15) Å], with eight molecules in the unit cell (Table S2 and Figure S5).

In the molecular packing of both structures, half of the molecules are oriented in a near-perpendicular arrangement relative to the other half, forming a well-organized architecture through numerous intermolecular interactions, including hydrogen bonds (primarily C—H···F, as well as C—H···N and C—H···O interactions) and C—H···π contacts, accompanied by weak π–π stacking interactions (Figure 2 and Figures S7 and S8).

2.3 | Thermal Properties

Compounds **1–4** are stable under ambient conditions and show no evidence of hydrolysis in dilute aprotic solutions (hexanes, toluene, chloroform, dichloromethane, acetone, acetonitrile). Thermogravimetric analysis (TGA) further indicates that these materials possess good thermal stability, with decomposition temperatures (T_d, defined as a 5% weight loss) of approximately 324°C, 293°C, 331°C, and 334°C for compounds **1**, **2**, **3**, and **4**, respectively (Figure S9).

2.4 | Electrochemical Properties

The positions of the HOMO and LUMO energy levels of compounds **1**, **2**, **3**, and **4** were determined using cyclic voltammetry (Figures S11–S14). The electrochemical studies demonstrated stable, reproducible cycles with well-defined anodic and cathodic peaks. This confirms the reversibility of the electron-transfer processes and the suitability of the materials' energy levels for applications in organic electronics; the calculated ionization potentials (5.18 eV for compound **1**, 5.16 eV for **2**, 5.20 eV for **3**, and 5.19 eV for **4**) and electron affinities (3.09, 3.10, 3.59, and 3.59 eV, respectively) (Table S4) agree with the photoluminescence (PL) data and confirm the charge-transfer nature of the excited states.

The HOMO energy levels of compounds **1–4** were also evaluated by ultraviolet photoelectron spectroscopy in air (UPS) (Figure S15). The ionization potentials were obtained by standard linear extrapolation of the rising edge of the photoemission spectra to the baseline. The resulting IP values −5.84 eV for compound **1**, 5.77 eV for **2**, 6.02 eV for **3**, and 5.94 eV for **4** (Table S4) – are higher than those derived from electrochemical measurements in solution, which is commonly attributed to solvation effects, polarization, and intermolecular interactions in the solid state.

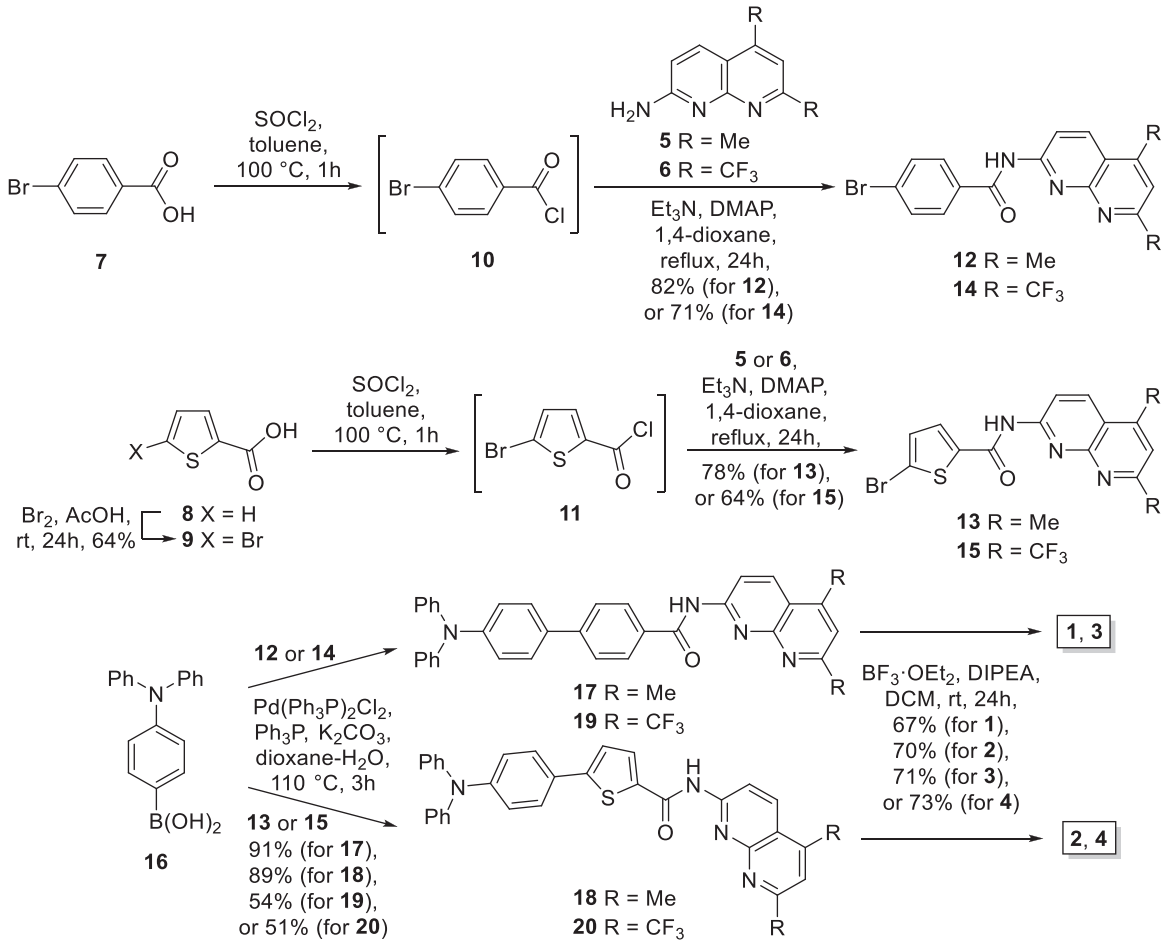

SCHEME 1 | Synthesis of boron difluoride complexes **1–4**.

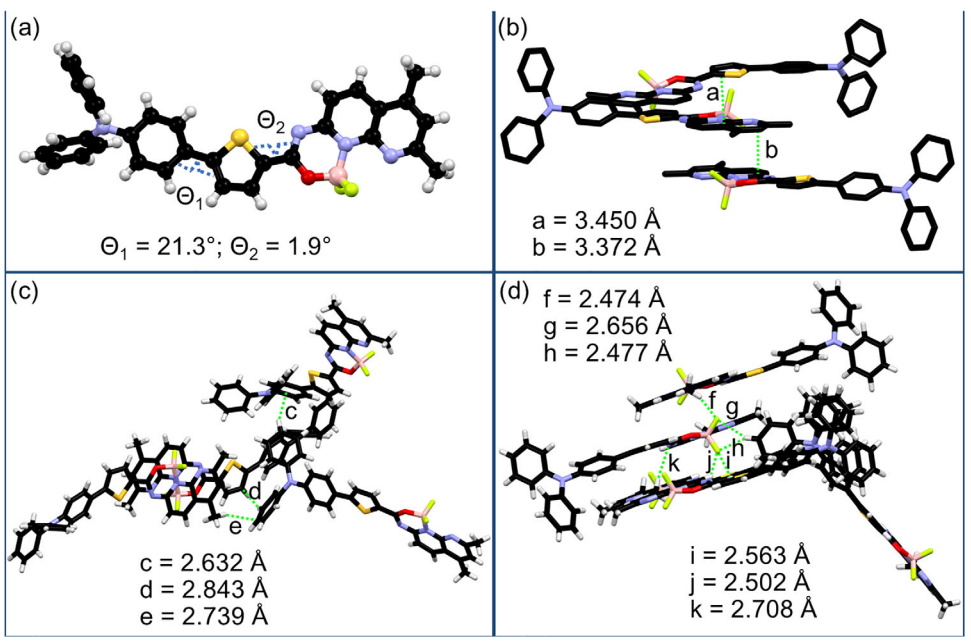

FIGURE 2 | X-ray molecular structures of compound **2** (a). Fragments of the crystal structures showing: π–π interactions (b) (hydrogen atoms are omitted for a clear view), CH···π (c), and CH···F/CH···N hydrogen bonds (d).

TABLE 1 | Hole and electron mobility parameters of compounds **1–4** at room temperature.

Dye	Electrons			Holes		
	μ_e (cm^2 V^{-1} s^{-1}) [a]	μ_0 (cm^2 V^{-1} s^{-1}) [b]	β (cm V^{-1})$^{1/2}$ [c]	μ_h (cm^2 V^{-1} s^{-1}) [a]	μ_0 (cm^2 V^{-1} s^{-1}) [b]	β (cm V^{-1})$^{1/2}$ [c]
1	3.9×10^{-5}	8.4×10^{-7}	0.0107	17×10^{-5}	8.4×10^{-7}	0.0067
2	1.2×10^{-5}	7.1×10^{-7}	0.0060	2.4×10^{-5}	7.1×10^{-7}	0.0045
3	0.9×10^{-6}	0.9×10^{-8}	0.0058	0.97×10^{-6}	3.6×10^{-9}	0.0070
4	2.4×10^{-6}	6.0×10^{-8}	0.0047	1.1×10^{-6}	1.3×10^{-9}	0.0086

[a]Electron (μ_e) and hole (μ_h) mobilities in an electric field of 6.4×10^5 V/cm.
[b]Zero-field mobilities (μ_0).
[c]Field dependence parameter (β) of a Poole–Frenkel type mobility ($\mu = \mu_0 e^{\alpha E^{1/2}}$). The thickness of the vacuum-evaporated layers varied from 0.763 to 1.203 μm (Figures S21–S24).

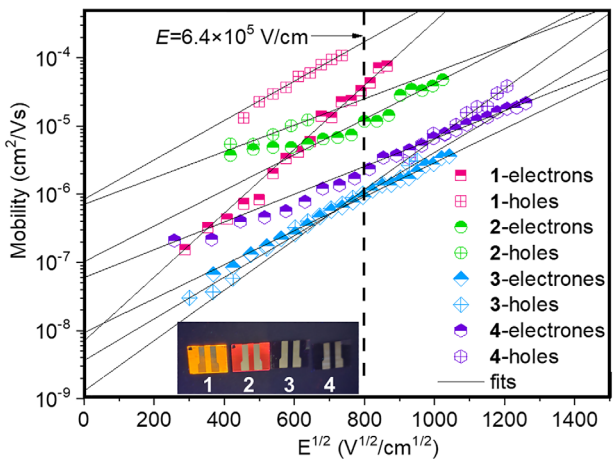

FIGURE 3 | Hole and electron mobilities as Poole–Frenkel functions of the electric field for compounds **1–4**. The dashed line indicates the electric field at which mobility values were collected in Table 1. The inset shows a photograph of the TOF samples of dyes **1–4** under UV excitation.

2.5 | Semiconducting Properties

The charge transport behavior of compounds **1–4** was investigated using the time-of-flight (TOF) technique. TOF measurements revealed bipolar charge transport in all BF_2 complexes **1–4**. Transit times were extracted from current transients plotted on log-log scales, enabling the determination of charge-carrier mobilities under various applied electric fields (Figure 3).

Both hole and electron mobilities of compounds **1–4** span a broad range from 5×10^{-8} to 1.7×10^{-4} cm^2 V^{-1} s^{-1}, depending on the electric field strength (Table 1). These results highlight the strong influence of molecular design and solid-state packing in vacuum-deposited films on the charge transport characteristics of the BF_2 complexes. Notably, the less polar complex **1** exhibited the highest hole (1.7×10^{-4} cm^2 V^{-1} s^{-1}) and electron (3.9×10^{-5} cm^2 V^{-1} s^{-1}) mobilities at an electric field of 6.4×10^5 V cm^{-1}, underscoring its potential for optoelectronic applications (Table 1).

In contrast, complex **3** displayed the most balanced charge transport, with comparable hole (9.7×10^{-7} cm^2 V^{-1} s^{-1}) and electron (9.0×10^{-7} cm^2 V^{-1} s^{-1}) mobilities at the same electric field, a feature that is particularly advantageous for OLED performance (Table 1). As expected from these features, similar transit times of approximately 100 μs were observed for holes and electrons in the vacuum-deposited film of compound **3** under applied positive and negative voltages of 80 V, respectively (Figure S19). Comparison of the corresponding current transients reveals a more pronounced plateau for electrons, indicating less dispersive electron transport relative to hole transport in this film. A similar trend was observed for the other studied boron complexes.

Overall, these findings demonstrate that the investigated BF_2 complexes represent a versatile platform not only for the development of efficient emissive materials but also for the design of advanced electron transport systems.

2.6 | Quantum Chemical Calculations

To gain insight into the electronic structure and excited-state characteristics of dyes **1–4**, DFT and TD-DFT calculations were carried out at the M06/def2-SVP level of theory. The optimized ground-state geometries reveal torsion angles between the triphenylamine donor and the *para*-phenylene/2,5-thienylene linker (Θ_1) of 30.2°–31.5° for compounds **1** and **3**, and 19.3°–20.5° for the thiophene-bridged analogues **2** and **4** (Figure 4). In contrast, the naphthyridino-oxadiazaborinine acceptor unit remains nearly coplanar with the *para*-phenylene/2,5-thienylene linker, exhibiting small torsion angles (Θ_2) of 0.4°–1.1°, which is favorable for effective π-conjugation and charge transport. These geometrical features are consistent with single-crystal X-ray diffraction data (Figure 2a and Figures S7a and S8a).

Frontier molecular orbital analysis shows that the HOMO is primarily localized on the triphenylamine donor moiety, whereas the LUMO is mainly distributed over the planar naphthyridino-oxadiazaborinine acceptor and the conjugated *para*-phenylene or 2,5-thienylene linker, with enhanced electron density toward the naphthyridine segment (Figure 4). This spatial separation of frontier orbitals supports efficient intramolecular charge transfer, which is beneficial for charge injection and exciton formation in OLED devices.

TD-DFT calculations indicate that the lowest-energy absorption bands arise from the $S_0 \rightarrow S_1$ transition and exhibit relatively high oscillator strengths (f = 0.7540, 1.0644, 0.4365, and 0.7059 for compounds **1**, **2**, **3**, and **4**, respectively; Table S5), implying strong light-harvesting capability. For the CF_3-substituted

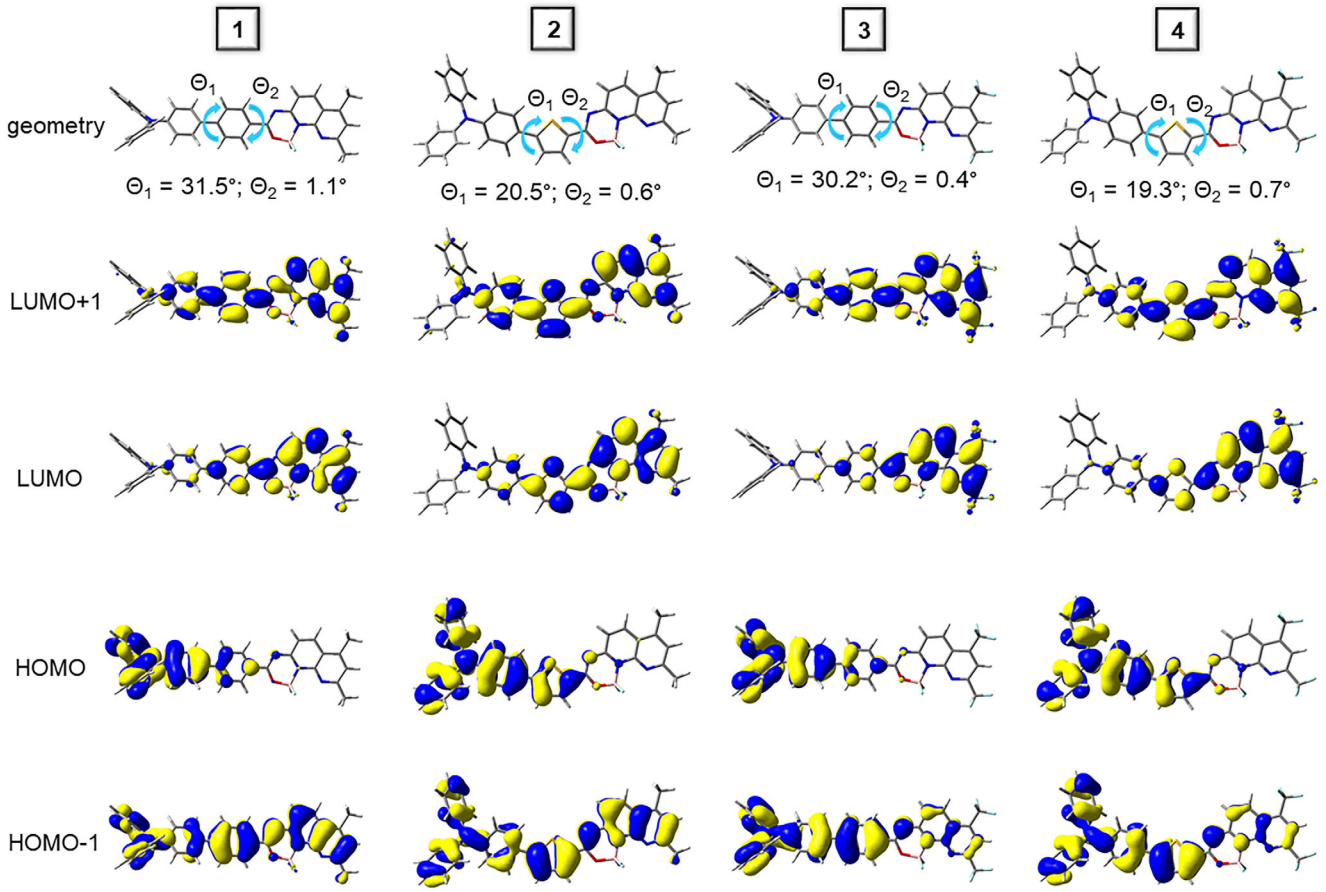

FIGURE 4 | Optimized ground-state structures and molecular orbitals of boron difluoride complexes **1–4**.

boron difluoride complexes **3** and **4**, the $S_0 \rightarrow S_1$ transition is dominated by HOMO→LUMO excitation, resulting in pronounced ICT character that is advantageous for red-emissive luminescence. By contrast, the CH_3-substituted analogues **1** and **2** exhibit mixed HOMO→LUMO, HOMO-1→LUMO, and HOMO→LUMO+1 contributions, indicating reduced ICT character. These differences in excited-state character rationalize the distinct photophysical behaviors observed experimentally.

2.7 | Photophysical Properties

We investigated the photophysical properties of dyes **1–4** in dilute solutions of *n*-hexane, toluene, chloroform, dichloromethane, acetone, and acetonitrile ($C = 2.0 \times 10^{-5}$ M). In apolar toluene, **1–4** exhibit broad low-energy absorption bands located at 424, 463, 483, and 520 nm, respectively (Figure 5a and Table 2). Apparently, replacing the 1,4-phenylene linker with 2,5-thienylene results in a bathochromic shift in the absorption spectra. An analogous effect is observed when methyl substituents on the naphthyridine units are replaced with trifluoromethyl groups.

Compounds **1**, **2**, **3**, and **4** all display broad PL bands in apolar toluene with maxima at 532, 546, 636, and 642 nm, respectively (Figure 5b and Table 2). Substituting methyl groups with trifluoromethyl groups on the naphthyridine unit induces a bathochromic shift of the emission from the green to the red region. This red shift is accompanied by a significant reduction in PLQY, from 84%–85% for emitters **1** and **2**% to 7% and 3% for the CF_3 analogues **3** and **4**, respectively. All investigated dyes show monoexponential decay kinetics and short nanosecond lifetimes in toluene solution (0.21–2.50 ns).

Overall, replacing the 1,4-phenylene linker with 2,5-thiophene and introducing CF_3 substituents effectively shifts the absorption and emission properties of the dyes towards lower energies. Although this enables a red emission, it also markedly reduces PLQY and the shortened luminescence lifetimes.

Next, we compared the absorption and PL properties of the four dyes in other solvents of varying polarity, namely *n*-hexane, chloroform, dichloromethane, acetone, and acetonitrile. The absorption spectra of all dyes show only minor changes in nonpolar *n*-hexane and medium-polarity chloroform and dichloromethane compared to those in toluene, while a slight hypsochromic shift is observed in the more polar acetone and acetonitrile solutions (Figures S25 and S26 and Table S6). In contrast, the emission properties are strongly dependent on solvent polarity. In nonpolar *n*-hexane, all four compounds exhibit hypsochromically shifted emission spectra (λ_{em} = 461, 496, 537, and 568 nm for dyes **1**, **2**, **3**, and **4**, respectively) compared to their toluene solutions. These spectra display a pronounced vibronic structure, and the PLQY values increase, particularly for dyes **3** and **4** to values of up to 66% and 46%, respectively. An increase in solvent polarity leads to bathochromic shifts of the emission bands and spectral broadening, accompanied by a significant decrease in PLQY.

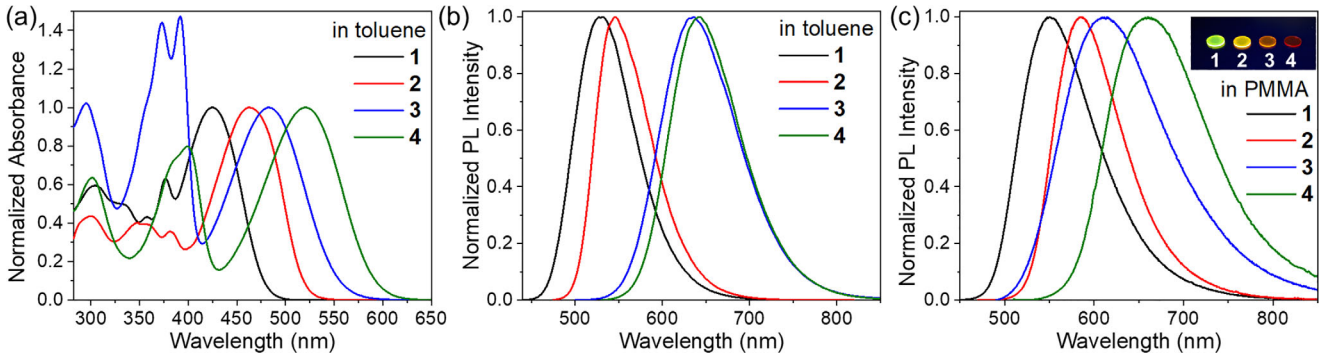

FIGURE 5 | Normalized absorption (a) and photoluminescence (b) spectra of solutions of dyes **1–4** in toluene ($C = 2.0 \times 10^{-5}$ M, λ_{ex} = 424, 462, 482, and 520 nm for dyes **1**, **2**, **3**, and **4**, respectively). Normalized photoluminescence spectra (c) of PMMA films of dyes **1–4** (1wt.% of dye, λ_{ex} = 420, 450, 480, and 490 nm for dyes **1**, **2**, **3**, and **4**, respectively). The inset shows a photograph of the film luminescence under UV excitation at 365 nm.

TABLE 2 | Photoluminescence properties of boron difluoride complexes **1–4** in toluene solutions and the PMMA-blended films.

Dye	In toluene				In PMMA		
	λ_{abs} (nm)[a]	λ_{em} (nm)[b]	PLQY (%)[c]	τ (ns)[d]	λ_{em} (nm)[b]	PLQY (%)[c]	τ (ns)[d]
1	424	532	84	2.5	550	100	3.5; 19.9
2	463	546	85	2.4	586	100	3.3; 7.2
3	483	636	7	0.87	614	30	2.2; 5.3
4	520	642	3	0.21	660	11	0.7; 1.9

[a]Absorption maximum at the longer wavelength (at 298 K at $C = 2.0 \times 10^{-5}$ M).
[b]Spectral position (wavelength) of the photoluminescence maximum (at 298 K at $C = 2.0 \times 10^{-5}$ M or in PMMA (1wt.% of dye)).
[c]Absolute photoluminescence quantum yield; [d] Photoluminescence lifetime.

Compounds **1** and **2** exhibit PLQYs of 72% and 77% in chloroform, 13% and 41% in dichloromethane, 1% and 3% in acetone, and less than 1% in acetonitrile (Table S6). The CF_3-substituted analogues **3** and **4** already show a very weak emission in chloroform with PLQY < 1% and no detectable emission in more polar solvents.

Then, we investigated the PL properties of compounds **1**, **2**, **3**, and **4** in dye films. The neat films of the dyes exhibit broad emission spectra, with maxima at 614, 644, 691, and 693 nm for compounds **1**, **2**, **3**, and **4**, respectively (Figure S27). The corresponding PLQY values are 17%, 12%, 3.3%, and 0.3%, respectively (Table S7).

To further assess the influence of a rigid environment on the photophysical behavior of dyes **1**, **2**, **3**, and **4**, we examined their photoluminescence properties in a polymer matrix. Poly(methyl methacrylate) (PMMA) was selected due to its excellent film-forming properties and high optical transparency. PMMA films containing 1 wt.% of each dye exhibit broad PL bands with maxima at 550, 586, 614, and 660 nm for dyes **1**, **2**, **3**, and **4**, respectively (Figure 5c and Table 2). Compared with the behavior observed in toluene solution, rigidification of the environment (despite its slightly higher polarity) leads to a substantial enhancement of the PLQY, reaching values of 100%, 100%, 30%, and 11% for compounds **1**, **2**, **3**, and **4**, respectively. Consequently, dyes bearing methyl substituents on the naphthyridine units (**1** and **2**) become highly emissive in a rigid matrix of moderate polarity such as PMMA. The CF_3-substituted analogues **3** and **4** also show a considerable improvement in PL efficiency, which can be attributed to the suppression of nonradiative decay pathways arising from restricted molecular rotation and vibrational motions within the PMMA matrix. The PL decay curves of these samples are best fitted by biexponential functions, with the shorter nanosecond-range lifetime component being dominant (Table 2 and Table S8). Furthermore, the PL properties of the films were examined as a function of temperature. Although compound **1** exhibits an increase in PL intensity upon heating from 77 to 300 K, and compounds **2** and **4** display similar behavior in the range of 77 to 180–200 K (Figure S28), their PL lifetimes remain nearly unchanged or even decrease slightly with increasing temperature (Figure S29 and Table S8). These observations indicate the absence of thermally activated delayed fluorescence (TADF) for dyes **1–4** in the polymeric environment.

To assess the potential of emitters **1–4** for optoelectronic applications, we investigated their PL properties in the semiconducting host material 1,3-bis(N-carbazolyl)benzene (mCP). The photoluminescence spectra exhibit bathochromic shifts relative to those recorded in toluene solution and in PMMA films, with emission maxima at 563, 592, 647, and 677 nm for dyes **1**, **2**, **3**, and **4**, respectively (Figure S30). This red shift is accompanied by a near-unity PLQY for emitters **1** and **2**, whereas the CF_3-substituted derivatives **3** and **4** reveal substantially lower PL efficiencies, with PLQY values of 7% and 3%, respectively. Analogously to PMMA films, the PL decay profiles of the dyes in the semiconducting matrix show two nanosecond-scale components (Table S9).

2.8 | Electroluminescent Properties

To assess the suitability of dyes **1–4** as OLED emitters, four distinct OLED architectures were systematically investigated: doping-free (**DF**), host-containing (**HC**), interface exciplex-forming (**EF**) devices, and devices featuring multiple ultrathin emissive layer configurations (**ML**). Each device type was fabricated using all dyes to enable a comprehensive comparison of their electroluminescent performance across different emission strategies.

The ionization energies (5.16–5.20 eV) and electron affinities (3.09–3.59 eV) of the emitters, determined by cyclic voltammetry measurements (Figures S11–S14, Table S4), were used to guide the rational design of the device architectures, ensuring efficient hole and electron injection into the emissive layers. The key electroluminescent characteristics of the **DF**, **HC**, **EF**, and **ML** devices are summarized in Table S10.

Notably, the explored device concepts enabled both a significant enhancement of the maximum external quantum efficiency of up to 12.76% for dye **1** and a pronounced bathochromic shift of the electroluminescence spectra to 688 nm for dye **4**. The performance characteristics of the **DF**, **HC**, **EF**, and **ML** devices are discussed in detail in the following subsections.

2.8.1 | Non-Doped OLEDs

In view of the bipolar charge-transport characteristics of complexes **1–4** (Table 1), a series of doping-free OLEDs (**DF-1**, **DF-2**, **DF-3**, and **DF-4**) incorporating neat light-emitting layers (EMLs) composed of materials **1**, **2**, **3**, and **4**, respectively, were fabricated and evaluated. The electroluminescence (EL) spectra of devices **DF-1**–**DF-4** exhibit broad emission bands with maxima at 596, 623, 635, and 668 nm for emitters **1**, **2**, **3**, and **4**, respectively (Figure S37 and Table S10). Notably, the EL spectra remain invariant over a wide range of operating voltages, indicating efficient exciton confinement within the EMLs and the absence of exciton leakage.

The progressive bathochromic shift observed in the EL spectra closely mirrors the corresponding trend in the PL spectra of emitters **1–4**, as discussed above. Furthermore, the evolution of the EQE – 2.80% for **DF-1**, 1.13% for **DF-2**, 0.58% for **DF-3**, and 0.05% for **DF-4** – correlates well with the PLQY trend of the respective emitters (Figure S38). Among the doping-free devices, **DF-1** exhibits the lowest turn-on voltage (4 V; Table S10), which is consistent with the superior hole and electron mobilities of compound **1** (Figure 3). Consequently, **DF-1** delivers the highest current and power efficiencies within the **DF** device series (Table S10).

2.8.2 | Host-Containing OLEDs

Considering the pronounced enhancement of the PLQYs of complexes **1–4** upon dispersion in the host mCP – reaching unity in the cases of emitters **1** and **2** – OLEDs with host-containing emitting layers (**HC-1**, **HC-2**, **HC-3**, and **HC-4**) were fabricated and investigated. These devices employed emissive layers composed of co-deposited mCP and emitters **1**, **2**, **3**, or **4**, respectively. Relative to the corresponding doping-free devices, the EL spectra of **HC-1** and **HC-2** exhibit pronounced hypsochromic shifts to 530 and 580 nm, respectively (Figures 6a and Figure S39 and Table S10). Such blue shifts are characteristic of CT-operated emitters dispersed in low-polarity environments [31].

In contrast, devices **HC-3** and **HC-4** show negligible spectral shifts upon host incorporation. This behaviour can be rationalized by the mechanochromic luminescence of emitters **3** and **4**, which leads to relaxation from different excited states in neat versus host-dispersed films. While the introduction of the host did not reduce the turn-on voltages compared with the DF devices (Figure 6b and Figure S40), it substantially improved device efficiencies. Specifically, maximum EQEs of 3.85%, 4.32%, 2.37%, and 1.14% were achieved for devices **HC-1**, **HC-2**, **HC-3**, and **HC-4**, respectively (Figure 6c and Figure S40b).

The observed efficiency enhancement can be partially attributed to effective triplet harvesting via TADF, as suggested by analyses of the PL decay dynamics (Figure S41). Notably, **HC-1** and **HC-2** display pronounced long-lived electroluminescence after the applied voltage is switched off (Figure 6d), which is indicative of delayed fluorescence. The minimal influence of reverse bias on the EL decay profiles suggests that charge transport does not play a significant role in delayed electroluminescence, supporting the conclusion that TADF under electrical excitation originates from triplet–singlet intersystem crossing.

Importantly, the maximum EQE values were achieved at relatively high luminance levels (Figure 6c and Figure S40), in agreement with time-of-flight (TOF) charge-transport measurements (Figure 3). These measurements reveal more balanced hole and electron mobilities at high electric fields compared with low-field conditions, thereby favoring efficient recombination at elevated luminance.

2.8.3 | Exciplex-Forming OLEDs

In the light of the relatively high turn-on voltages observed for the **DF** and **HC** devices, an exciplex-forming interface strategy was adopted to fabricate OLEDs **EF-1**, **EF-2**, **EF-3**, and **EF-4** incorporating compounds **1–4** and the host mCP, respectively. This approach has recently proven highly effective, enabling the realization of white OLEDs with exceptionally low turn-on voltages (as low as 2.51 V), high power efficiencies (up to 85.8 lm W^{-1}), and even high-speed visible-light communication with data rates reaching 14 Mbps [32]. More broadly, many state-of-the-art OLEDs exploit exciplex-forming systems to facilitate efficient host–guest energy transfer and effective triplet harvesting through the TADF of the exciplex [33–36].

To ensure efficient energy transfer to the emitter, a sky-blue exciplex-forming donor–acceptor pair composed of mCP and PO-T2T [37–39] was selected. This choice was guided by the substantial spectral overlap between the exciplex emission of the solid-state mCP/PO-T2T mixture and the absorption spectra of compounds **1–4** (Figure S42). In the **EF** device architecture, the exciplex is formed at the interface between the light-emitting layer comprising dye **1–4** (10 wt.%):mCP and the

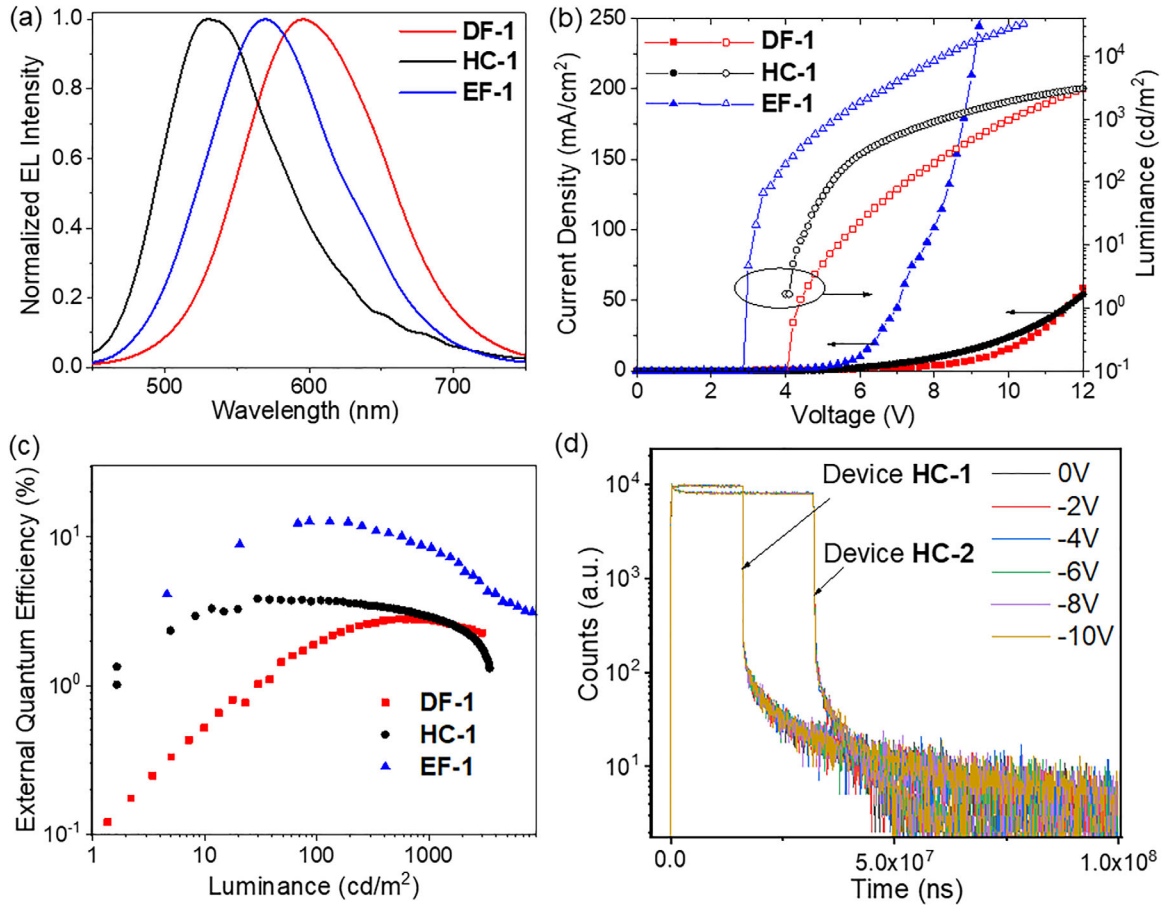

FIGURE 6 | Normalized EL spectra (a) recorded at 10 V, current density and luminance versus voltage plots (b), plots of EQE versus luminance (c) for devices **DF-1**, **HC-1,** and **EF-1** containing the same emitter **1**. EL decay curves (d) of devices **HC-1** and **HC-2** at different voltage pulse set-on.

electron-transporting layer PO-T2T (Figure S35). Notably, the characteristic sky-blue exciplex emission is absent from the **EL** spectra of the **EF** devices (Figure S41), which are instead dominated by emission from the dyes, confirming efficient exciton and energy transfer from the exciplex to the emitters.

This interfacial exciplex functions as an "active heterostructure," [40] effectively reducing the energy barriers for charge injection and thereby lowering the turn-on voltages of the **EF** devices (Figure S43). For instance, device **EF-1** exhibits a turn-on voltage of 2.8 V, significantly lower than the 4.0 V observed for the corresponding **DF-1** and **HC-1** devices employing the same emitter (Figure 6b and Table S10). Moreover, exciplex-based devices containing emitters **1** and **2** achieve pronounced enhancements in external quantum efficiency, reaching 12.76% and 6.16%, respectively, compared with 3.85% and 4.32% for devices **HC-1** and **HC-2** (Figure S43 and Table S10).

The superior performance of devices **EF-1** and **EF-2** can be attributed to the synergistic combination of several factors: (i) high and well-balanced hole and electron mobilities of compounds 1 and 2; (ii) the intrinsic TADF characteristics of emitters **1** and **2**, as evidenced by their photoluminescence decay profiles in a PMMA host; (iii) efficient TADF of the mCP/PO-T2T exciplex, as reported previously; and (iv) enhanced charge injection facilitated by the active interfacial heterostructure formed at the **1–4** (10 wt.%):mCP/PO-T2T junction.

In contrast, this strategy is less effective for compounds **3** and **4**, primarily due to their comparatively low charge-carrier mobilities (Figure 3). Consequently, devices **EF-3** and **EF-4** exhibit maximum EQEs of 2.37% and 1.14%, respectively, which are comparable to those of **HC-3** (2.30%) and **HC-4** (0.57%) and do not represent a significant improvement. These results underscore the need for alternative device-design strategies tailored to red emitters, as discussed in the following subsection.

2.8.4 | OLEDs With Multiple Ultrathin Emissive Layer Configurations

Based on the PL spectra of the neat films (Figure S27), compounds **3** and **4** emerge as promising emitters for far-red OLED applications. However, when dispersed in PMMA or mCP hosts, both compounds exhibit pronounced blue-shifted PL spectra relative to their neat films (Figure 5c and Figure S30). This behavior is characteristic of many emitters used to enhance the efficiency of host-containing deep-red OLEDs, but it inevitably compromises emission wavelengths by shifting the emission towards shorter wavelengths in the host environment [41, 42].

To overcome this limitation, an alternative device-design strategy was employed, based on ultrathin emitter layers incorporated into multiple ultrathin emissive layer configurations for the fabrication of deep-red and NIR OLEDs. These configurations

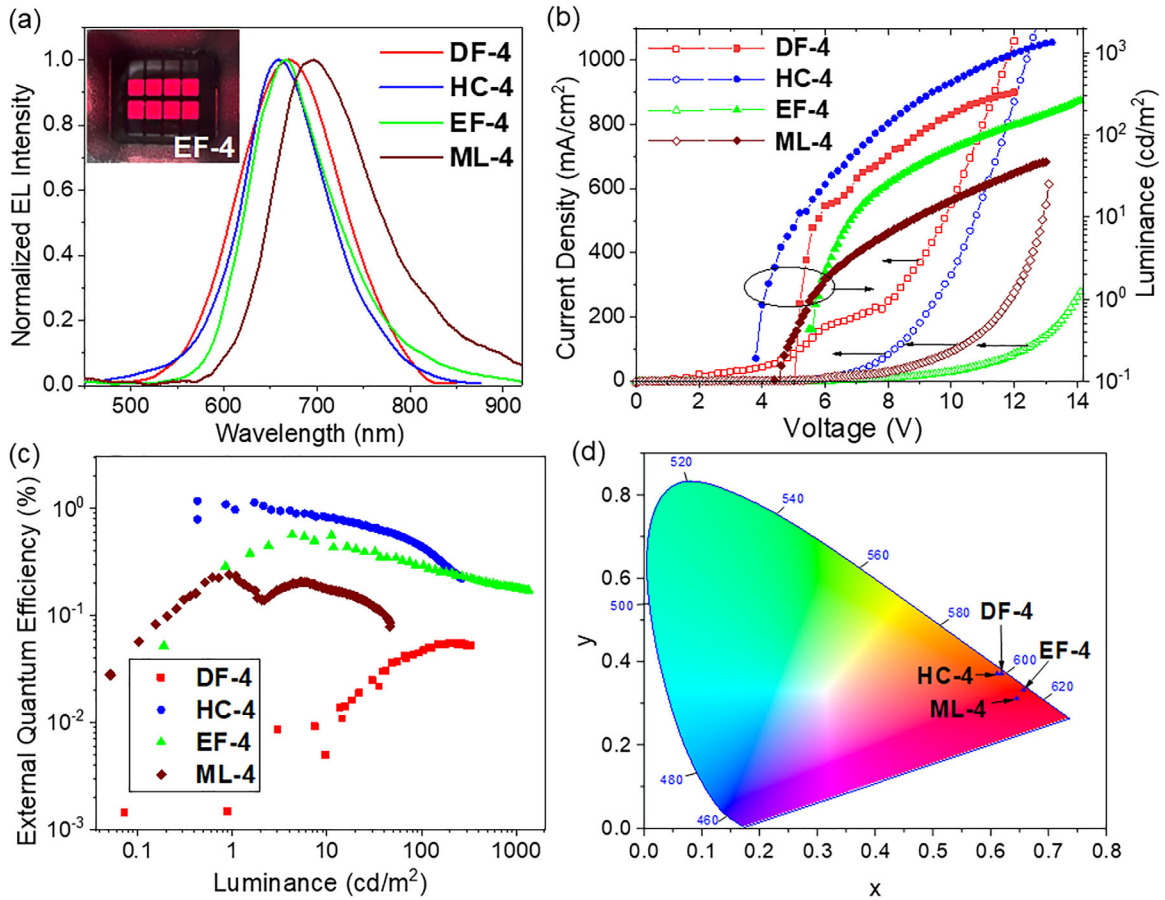

FIGURE 7 | Electroluminescence characteristics of devices containing emitter **4**. Normalized EL spectra (a) recorded at 10 V (the inset shows a photo of device **EF-4** under applied voltage); corresponding current density and luminance versus voltage plots (b); plots of EQE versus luminance (c); Commission Internationale de l'Éclairage (CIE) 1931 chromaticity coordinates (d).

resemble the structure of devices with multi-quantum-well architectures [43–45]; however, quantum confinement effects were not observed in this study. It should be noted that OLEDs employing doping-free, multilayered emissive structures with TADF in the far-red/NIR region have been reported [46] to exhibit enhanced external quantum efficiencies compared to their reference, i.e., conventional doping-free TADF OLEDs [47].

In line with these reports, similar performance trends were observed for the performance of devices **ML-3** and **ML-4** incorporating emitters **3** and **4**, respectively (Figures 7 and Figure S44 and Table S10).

Amongst the investigated devices, **ML-4**, based on dye **4**, displays the most pronounced bathochromic electroluminescence (Figure 7a). Its CIE 1931 color coordinates are shifted further into the deep-red region compared with those of devices **DF-4**, **HC-4**, and **EF-4** using the same emitter (Figure 7b). Specifically, device **ML-4** exhibits an EL peak at 688 nm and CIE 1931 coordinates of (0.645, 0.311), satisfying the criteria for far-red emitters (emission wavelength > 650 nm, $x \geq 0.60$, $y \leq 0.40$) [48, 49]. As expected, devices based on dye **4** exhibit relatively low maximum luminance, reflecting the reduced sensitivity of the human eye in the far-red spectral region (Figure 7c and Table S10).

Although device **ML-4** exhibits a lower maximum EQE than the corresponding **HC-4** and **EF-4** devices, its efficiency surpasses that of the doping-free **DF-4** device. These results highlight the utility of the ML approach for the development of far-red and NIR OLEDs when emitters display a high emissive efficiency in neat films. Importantly, this strategy preserves far-red electroluminescence by suppressing the host-induced blue shift that commonly accompanies conventional hosting approaches.

3 | Conclusion and Outlook

We report the synthesis and comprehensive spectroscopic investigation of four donor–acceptor boron difluoride complexes **1–4** incorporating a triphenylamine electron donor and a naphthyridine-fused [1, 3, 5, 2]oxadiazaborinine acceptor. Charge-transport studies reveal balanced hole and electron mobilities, highlighting the potential of these materials as a versatile platform for the development of efficient emissive systems and electron-transporting materials. Photophysical investigations in aprotic solvents of varying polarity show a pronounced red shift of the emission spectra, accompanied by a decrease in fluorescence intensity with increasing solvent polarity, indicative of a strong intramolecular charge transfer (ICT) character. Compounds **1** and **2** exhibit near-unity photoluminescence

quantum yields when embedded in PMMA and mCP matrices, demonstrating excellent solid-state emissive performance. In contrast, the CF_3-substituted analogues **3** and **4** display significant bathochromic shifts accompanied by a reduced emission intensity.

The presence of trifluoromethyl groups in compounds **3** and **4** significantly enhances ICT character by stabilizing the LUMO and promoting a dominant HOMO→LUMO transition, as confirmed by TD-DFT calculations. This leads to a strongly polarized excited state with a reduced S_1–S_0 energy gap and increased geometric relaxation. Under these conditions, nonradiative decay is effectively governed by the energy gap law, resulting in enhanced internal conversion and reduced photoluminescence efficiency. In contrast, the CH_3-substituted analogues **1** and **2** exhibit weaker ICT character with mixed excited-state configurations, larger energy gaps, and reduced structural relaxation, which suppress nonradiative decay and enable higher radiative efficiency, consistent with their high PLQY values.

All four dyes were successfully implemented as emitters in various OLED architectures, including doping-free (**DF**), host-containing (**HC**), and interface exciplex-forming (**EF**), and devices with multiple ultrathin emissive layer (**ML**) configurations, and were systematically evaluated. EF-OLEDs demonstrate external quantum efficiency of up to 12.76%. Notably, compounds **3** and **4** were further employed in **ML** devices to fabricate far-red OLEDs, achieving electroluminescence maxima at 650 and 688 nm, respectively. These results demonstrate the strong potential of this class of boron difluoride complexes for tunable emission and diverse optoelectronic applications.

4 | Experimental Section

4.1 | General

4.1.1 | Materials

All reagents and chemicals (at least analytical grade) were purchased from commercial sources (TCI, Aldrich, or Acros Organics) and used without further purification. For OLED fabrication, commercially available materials delivered by Ossila Ltd. were employed, including hole-injecting layers based on dipyrazino[2,3-f:2′,3′-h]quinoxaline-2,3,6,7,10,11-hexacarbonitrile (HAT-CN) or copper(I) iodide (CuI); hole-transporting materials 4,4′-cyclohexylidenebis[*N*,*N*-bis(4-methylphenyl)benzenamine] (TAPC) and tris(4-carbazoyl-9-ylphenyl)amine (TCTA); the host material mCP; the hole/exciton-blocking material diphenyl[4-(triphenylsilyl)phenyl]phosphine oxide (TSPO1) and 2,4,6-tris[3-(diphenylphosphinyl)phenyl]-1,3,5-triazine (PO-T2T); the electron-transporting material 2,2′,2″-(1,3,5-benzinetriyl)-tris(1-phenyl-1*H*-benzimidazole) (TPBi) (Figure S32); and lithium fluoride (LiF) as the electron-injecting layer.

4.1.2 | Instrumental Methods

4.1.2.1 | Structural Characterization. NMR spectra were recorded on a Varian Mercury 400 MHz (at 400 and 101 MHz for ^{1}H and ^{13}C NMR spectra, respectively), Varian V NMRS 500 MHz (at 500, 125, and 470 MHz for ^{1}H, ^{13}C, and ^{19}F NMR spectra, respectively), or Varian V NMRS 600 MHz (at 600 and 151 MHz for ^{1}H and ^{13}C NMR spectra, respectively) spectrometers at room temperature using $CDCl_3$ or DMSO-d_6 as a solvent, and referenced externally to $SiMe_4$. The multiplicities of the signals are indicated as "s," "d," "t," or "m", which stand for singlet, doublet, triplet, and multiplet, respectively. High-resolution mass spectra (HRMS) were collected on a Synapt G2-S HDMS (Waters Inc.) mass spectrometer equipped with an electrospray ion source and a q-TOF-tupe mass analyser. The instrument was controlled, and the recorded data were processed using MassLynx 4.1 software package (Waters Inc., USA).

4.1.2.2 | Single Crystal X-Ray Diffraction Analysis. Single crystals of boron complexes were grown by slow evaporation of their solution in toluene (structure **1**) or dichloromethane (structures **2** and **4**) under ambient conditions. The X-ray measurements were performed on a SuperNova Agilent diffractometer using CuKα (λ = 1.54184 Å) radiation at 100 K. Data reduction was done with *CrysAlisPro* [50]. The obtained structures were solved by direct methods and refined using *SHELXL* [51] under *WinGX* [52]. Crystallographic data of compounds **1**, **2**, and **4** have been deposited with the Cambridge Crystallographic Data Centre (CCDC) and can be obtained, free of charge, from CCDC via https://www.ccdc.cam.ac.uk/structures/.

4.1.2.3 | Thermal Analysis. The thermogravimetric measurements were performed on TGA/DSC 3+, Mettler Toledo apparatus at a heating rate of 5°C/min under nitrogen atmosphere. DSC measurements were done on DSC 3, Mettler Toledo equipment at a heating rate of 5°C/min under a nitrogen atmosphere.

4.1.2.4 | *Cyclic voltammetry.* *Cyclic voltammetry* was performed in a three-electrode cell with Ag/AgCl as the reference electrode, a glassy carbon working electrode, and a platinum wire as the counter electrode. The measurements were carried out in dry dichloromethane with tetrabutylammonium hexafluorophosphate as the supporting electrolyte, and the onset oxidation and reduction potentials obtained from the voltammograms were used to calculate the ionization potential and electron affinity.

4.1.2.5 | Charge-Transporting Measurements. The drift charge transport characteristics of the investigated dyes were studied using the TOF and CELIV techniques. The EKSPLA NL300 laser (excitation wavelength of 355 nm), the 6517B electrometer (Keithley), function generator AFG3011C (Tektronix), and the TDS 3032C oscilloscope (Tektronix) were used to test films made through thermal vacuum deposition, with positive or negative voltages (U) applied.

4.1.2.6 | Theoretical Calculations. The ground-state geometries of molecules **1–4** were fully optimized by the M06 method and def2svp basic sets with the inclusion of toluene solvent effect through the conductor-like polarizable continuum model (CPCM) using the Gaussian 16 software package [53]. Molecular orbitals were visualized with Gaussview 6.0 [54].

4.1.2.7 | Photophysics. UV–vis spectra in solutions were recorded on a Shimadzu UV2700 spectrophotometer at room temperature. Steady-state fluorescence emission spectra for both ca. 10^{-5} M solutions and thin solid films were performed at room temperature on an Edinburgh Instruments Spectrophotometer (FS5, Edinburgh, UK) with a xenon lamp as the light source. The absolute photoluminescence quantum yields were measured with a calibrated SC-30 Integrating Sphere and were excited at the appropriate absorption wavelength in each case. Thin film samples were fabricated on the precleaned quartz plates by using the spin-coating technique utilizing SPSEurope Spin150 Spin processor using 2.5 mg/mL solutions of the complexes in DCM. Fluorescence decays of the solutions and of the solid-state samples were recorded with a 374 nm PicoQuant LDH-D-C-375 laser as an excitation source using the time-correlated single photon counting technique for detection.

4.1.2.8 | Device Fabrications. All OLEDs shared a common multilayer device architecture consisting of an anode (100 nm)/hole-injecting layer (5 nm)/hole-transporting layer (40 nm)/exciton-blocking layer (10 nm)/light-emitting layer (25 nm)/exciton-blocking layer (10 nm)/electron-transporting layer (30 nm)/electron-injecting layer (0.7 nm)/cathode (120 nm). The detailed layer compositions and corresponding energy level diagrams for **DF**, **HC**, **EF**, and **QW** devices are schematically illustrated in Figures S33–S35. OLED devices were fabricated on glass substrates coated with indium tin oxide (ITO) and 100 nm thick. Before evaporation, the substrates were washed with distilled water, then with acetone, followed by sonication in acetone. The layers were thermally deposited using a vacuum chamber at a pressure of 10^{-5} Torr. The fabricated devices had a pixel area of 2 × 2 mm. The devices were characterized using a Hewlett-Packard Semiconductor parameter analyzer 4145A and a calibrated photodiode. The spectra were measured on an Ocean Optics USB2000 spectrometer.

4.2 | Synthesis

4.2.1 | 5-Bromothiophene-2-Carboxylic Acid (9)

Thiophene-2-carboxylic acid (**8**, 5.00 g, 39.02 mmol, 1.0 equiv) was dissolved in acetic acid (90 mL), and a solution of bromine (6.24 g, 39.02 mmol, 1.0 equiv) in acetic acid (10 mL) was added dropwise over 15 min. The reaction mixture was stirred at room temperature for 24 h. The solvent was then removed under reduced pressure, and water (50 mL) was added to the residue. The resulting precipitate was filtered, washed with water, and dried to afford the desired compound in 64% yield (5.18 g, 25.02 mmol). The product was further used without additional purification. ^{1}H NMR (400 MHz, DMSO-d_6): δ = 13.40 (1H, s, OH), 7.55 (1H, d, J = 4.0 Hz, thiophene-H), 7.32 (1H, d, J = 3.9 Hz, thiophene-H) ppm. ^{13}C{H} NMR (101 MHz, DMSO-d_6): δ = 161.77, 136.15, 133.89, 131.89, 118.86 ppm.

4.2.2 | General Procedure A: Synthesis of Amides 12–15

Thionyl chloride (132–187 µL, 1.82–2.57 mmol, 1.5 equiv) was added to a suspension of 4-bromobenzoic acid (**7**, 262–302 mg, 1.30–1.50 mmol, 1.0 equiv) or 5-bromothiophene-2-carboxylic acid (**9**, 251–355 mg, 1.21–1.71 mmol, 1.0 equiv) in dry toluene (10 mL). The reaction mixture was heated at 100°C for 1 h. After cooling, the solvent and the rest of the thionyl chloride were evaporated in a vacuum. Such obtained 4-bromobenzoyl chloride (**10**) or 5-bromothiophene-2-carbonyl chloride (**11**) was dissolved in dry 1,4-dioxane (10 mL). Then 5,7-dimethyl-1,8-naphthyridin-2-amine (**5**, 210–226 mg, 1.21–1.31 mmol, 1.0 equiv) or 5,7-bis(trifluoromethyl)-1,8-naphthyridin-2-amine (**6**, 422–482 mg, 1.50–1.71 mmol, 1.0 equiv), dry triethylamine (507–717 µL, 3.64–5.14 mmol, 3.0 equiv), and DMAP (7–10 mg, 0.06–0.09 mmol, 0.05 equiv) were added. Next, the reaction mixture was refluxed for 24 h. After cooling, water (20 mL) and the saturated aqueous solution of $NaHCO_3$ (20 mL) were added, and the mixture was extracted with DCM (3 × 40 mL). The combined organic layers were dried over anhydrous Na_2SO_4, filtered, and concentrated. The crude product was purified by flash column chromatography on silica gel (DCM/methanol from 100:0 to 97:3, v/v, for compounds **12** and **13**; or hexanes/DCM from 4:1 to 1:2, v/v, for compounds **14** and **15**).

4-Bromo-*N*-(5,7-dimethyl-1,8-naphthyridin-2-yl)benzamide (12) was obtained as a white crystalline solid in 82% yield (381 mg) using general procedure A from acid **7** (262 mg, 1.30 mmol) and amine **5** (226 mg, 1.30 mmol). ^{1}H NMR (400 MHz, DMSO-d_6): δ = 11.40 (1H, s, NH), 8.54 (1H, d, J = 9.0 Hz, naphthyridine-H), 8.39 (1H, d, J = 9.0 Hz, naphthyridine-H), 8.03 (2H, d, J = 8.6 Hz, Ar-H), 7.74 (2H, d, J = 8.6 Hz, Ar-H), 7.27 (1H, s, naphthyridine-H), 2.64 (3H, s, CH_3), 2.61 (3H, s, CH_3). ^{13}C{H} NMR (101 MHz, DMSO-d_6): δ = 165.78, 162.08, 154.53, 153.78, 145.48, 135.81, 133.04, 131.41 (2C), 130.35 (2C), 126.08, 122.01, 118.14, 114.32, 25.16, 17.57 ppm. HRMS (ESI-TOF) calculated for $C_{17}H_{14}BrN_3ONa$ $[M + Na]^+$: 378.0218, found: 378.0219.

5-Bromo-*N*-(5,7-dimethyl-1,8-naphthyridin-2-yl)thiophene-2-carboxamide (13) was obtained as a white crystalline solid in 78% yield (343 mg) using general procedure A from acid **9** (251 mg, 1.21 mmol) and amine **5** (210 mg, 1.21 mmol). ^{1}H NMR (400 MHz, DMSO-d_6): δ = 11.51 (1H, s, NH), 8.52 (1H, d, J = 9.0 Hz, naphthyridine-H), 8.32 (1H, d, J = 9.0 Hz, naphthyridine-H), 8.17 (1H, d, J = 4.1 Hz, thiophene-H), 7.38 (1H, d, J = 4.1 Hz, thiophene-H), 7.26 (1H, s, naphthyridine-H), 2.63 (3H, s, CH_3), 2.60 (3H, s, CH_3) ppm. ^{13}C{H} NMR (101 MHz, DMSO-d_6): δ = 162.17, 159.88, 154.51, 153.39, 145.52, 141.14, 135.95, 132.11, 131.46, 122.04, 119.23, 118.13, 114.13, 25.20, 17.56 ppm. HRMS (ESI-TOF) calculated for $C_{15}H_{13}BrN_3OS$ $[M + H]^+$: 361.9963, found: 361.9965.

***N*-[5,7-Bis(trifluoromethyl)-1,8-naphthyridin-2-yl]-4-bromobenzamide (14)** was obtained as a white crystalline solid in 71% yield (496 mg) using general procedure A from acid **7** (302 mg, 1.50 mmol) and amine **6** (422 mg, 1.50 mmol). ^{1}H NMR (400 MHz, $CDCl_3$): δ = 9.20 (1H, s, NH), 8.96 (1H, d, J = 9.3 Hz, naphthyridine-H), 8.63 (1H, dd, J = 9.3 Hz, J = 1.8 Hz, naphthyridine-H), 8.02 (1H, s, naphthyridine-H), 7.84 (2H, d, J = 8.5 Hz, Ar-H), 7.69 (2H, d, J = 8.5 Hz, Ar-H) ppm. ^{13}C{H} NMR (101 MHz, $CDCl_3$): δ = 165.34, 155.61, 154.65, 151.27 (1C, q, $J_{C\text{-}F}$ = 36.6 Hz, C-CF_3), 138.10 (1C, q, $J_{C\text{-}F}$ = 33.3 Hz, C-CF_3), 136.09, 132.61 (2C), 132.01, 129.09 (2C), 128.45, 122.01 (1C, q, $J_{C\text{-}F}$ = 275.4 Hz, CF_3), 120.62 (1C, q, $J_{C\text{-}F}$ = 275.8 Hz, CF_3), 118.77, 117.45, 113.83 ppm. ^{19}F NMR (376 MHz, $CDCl_3$): δ = -60.82 (3F, s, CF_3), -68.07 (3F, s, CF_3) ppm. HRMS (ESI-TOF) calculated for $C_{17}H_8N_3OF_6BrNa$ $[M + Na]^+$: 485.9653, found: 485.9641.

***N*-(5,7-Bis(trifluoromethyl)-1,8-naphthyridin-2-yl)-5-bromothiophene-2-carboxamide (15)** was obtained as a white crystalline solid in 64% yield (518 mg) from acid **9** (355 mg, 1.71 mmol) and amine **6** (482 mg, 1.71 mmol) using general procedure A. ^{1}H NMR (400 MHz, $CDCl_3$): δ = 8.86–8.91 (2H, m, NH, naphthyridine-H), 8.61 (1H, d, J = 9.3 Hz, naphthyridine-H), 8.02 (1H, s, naphthyridine-H), 7.47 (1H, d, J = 4.0 Hz, thiophene-H), 7.17 (1H, d, J = 4.0 Hz, thiophene-H) ppm. ^{13}C{H} NMR (101 MHz, $CDCl_3$): δ = 159.31, 155.26, 154.64, 151.31 (1C, q, $J_{C\text{-}F}$ = 36.2 Hz, C-CF_3), 139.24, 138.11 (1C, q, $J_{C\text{-}F}$ = 32.9 Hz, C-CF_3), 136.11, 131.59, 130.06, 122.37 (1C, q, $J_{C\text{-}F}$ = 275.3 Hz, CF_3), 121.80, 120.61 (1C, q, $J_{C\text{-}F}$ = 276 Hz, CF_3), 118.71, 117.42, 113.83 ppm. ^{19}F NMR (376 MHz, $CDCl_3$): δ = -60.82 (3F, s, CF_3), -68.09 (3F, s, CF_3) ppm. HRMS (ESI-TOF) calculated for $C_{15}H_6BrF_6N_3OSNa$ [M + Na]$^+$: 491.9217, found: 491.9213.

4.2.3 | General Procedure B: Synthesis of Ligands 17–20

A mixture of bromo derivatives **12–15** (0.72–1.03 mmol, 1.0 eqiuv), [4-(diphenylamino)phenyl]boronic acid (**16**, 314–447 mg, 1.08–1.55 mmol, 1.5 equiv), triphenylphosphine (19–27 mg, 0.07–0.10 mmol, 0.1 equiv), and potassium carbonate (297–424 mg, 2.17–3.09 mmol, 3.0 equiv) were suspended in 1,4-dioxanewater mixture (40:16 mL) and degassed with a stream of argon passing through the solution for 15 min. Then, $Pd(Ph_3P)_2Cl_2$ (25–36 mg, 0.04–0.05 mmol, 0.05 equiv) was added, and the reaction mixture was stirred under an argon atmosphere for 3 h at 105°C. After cooling, water (30 mL) was added, and the mixture was extracted with DCM (4 × 50 mL). The collected organic phases were dried over Na_2SO_4, filtered, and concentrated under reduced pressure. The residue was purified by flash chromatography on silica gel (DCM/methanol = 100:0 to 99:1, v/v for compounds **17** and **18**; and hexanes/DCM = 2:1 to 1:4, v/v for compounds **19** and **20**) to give products **17–20**.

***N*-(5,7-Dimethyl-1,8-naphthyridin-2-yl)-4'-(diphenylamino)-[1,1'-biphenyl]-4-carboxamide (17)** was obtained as a yellow crystalline solid in 91% yield (352 mg) using general procedure B from bromo-derivative **12** (264 mg, 0.74 mmol). ^{1}H NMR (600 MHz, DMSO-d_6): δ = 11.29 (1H, s, NH), 8.55 (1H, d, J = 9.0 Hz, naphthyridine-H), 8.44 (1H, d, J = 9.0 Hz, naphthyridine-H), 8.17 (2H, d, J = 8.1 Hz, Ar-H), 7.80 (2H, d, J = 8.3 Hz, Ar-H), 7.71 (2H, d, J = 8.7 Hz, Ar-H), 7.33–7.36 (4H, m, Ar-H), 7.27 (1H, s, naphthyridine-H), 7.08–7.11 (6H, m, Ar-H), 7.05 (2H, d, J = 8.7 Hz, Ar-H), 2.65 (3H, s, CH_3), 2.61 (3H, s, CH_3) ppm. ^{13}C{H} NMR (151 MHz, DMSO-d_6): δ = 166.18, 161.99, 154.57, 153.98, 147.50, 146.85 (2C), 145.46, 143.04, 135.70, 132.30, 131.92, 129.67 (4C), 128.95 (2C), 127.88 (2C), 125.81 (2C), 124.48 (4C), 123.55 (2C), 122.71 (2C), 121.92, 118.07, 114.42, 25.15, 17.57 ppm. HRMS (ESI-TOF) calculated for $C_{35}H_{29}N_4O$ [M + H]$^+$: 521.2341, found: 521.2346.

***N*-(5,7-Dimethyl-1,8-naphthyridin-2-yl)-5-(4-(diphenylamino)phenyl)thiophene-2-carboxamide (18)** was obtained as a yellow crystalline solid in 89% yield (340 mg) using general procedure B from bromo-derivative **14** (262 mg, 0.72 mmol). ^{1}H NMR (600 MHz, DMSO-d_6): δ = 11.39 (1H, s, NH), 8.53 (1H, d, J = 9.1 Hz, naphthyridine-H), 8.38 (1H, d, J = 9.0 Hz, naphthyridine-H), 8.31 (1H, d, J = 4.0 Hz, thiophene-H), 7.65 (2H, d, J = 8.7 Hz, Ar-H), 7.50 (1H, d, J = 4.0 Hz, thiophene-H), 7.33–7.36 (4H, m, Ar-H), 7.26 (1H, s, naphthyridine-H), 7.07–7.12(6H, m, Ar-H), 6.98 (2H, d, J = 8.7 Hz, Ar-H), 2.64 (3H, s, CH_3), 2.61 (3H, s, CH_3) ppm. ^{13}C{H} NMR (151 MHz, DMSO-d_6): δ = 162.07, 160.80, 154.60, 153.67, 149.75, 147.90, 146.62 (2C), 145.49, 136.95, 135.84, 131.98, 129.73 (4C), 127.03 (2C), 126.40, 124.70 (4C), 123.83 (2C), 123.70, 122.28 (2C), 121.92, 118.03, 114.20, 25.19, 17.51 ppm. HRMS (ESI-TOF) calculated for $C_{33}H_{27}N_4OS$ [M + H]$^+$: 527.1906, found: 527.1910.

***N*-(5,7-Bis(trifluoromethyl)-1,8-naphthyridin-2-yl)-4'-(diphenylamino)-[1,1'-biphenyl]-4-carboxamide (19)** was obtained as an orange crystalline solid in 54% yield (307 mg) using general procedure B from bromo-derivative **13** (418 mg, 0.90 mmol). ^{1}H NMR (500 MHz, $CDCl_3$): δ = 9.20 (1H, s, NH), 9.03 (1H, d, J = 9.3 Hz, naphthyridine-H), 8.63 (1H, dd, J = 1.79 Hz, J = 9.37 Hz, naphthyridine-H), 8.01–8.03 (3H, m, Ar-H, naphthyridine-H), 7.72–7.74 (2H, m, Ar-H), 7.52–7.55 (2H, m, Ar-H), 7.28–7.31 (4H, m, Ar-H), 7.15–7.17 (6H, m, Ar-H), 7.06–7.09 (2H, m, Ar-H) ppm. ^{13}C{H} NMR (125 MHz, $CDCl_3$): δ = 165.90, 155.87, 154.79, 151.17 (1C, q, $J_{C\text{-}F}$ = 36.3 Hz, C-CF_3), 148.56, 147.49 (2C), 145.65, 138.03 (1C, q, $J_{C\text{-}F}$ = 33.0 Hz, C-CF_3), 135.92, 132.66, 130.93, 129.54 (4C), 128.16 (2C), 128.06 (2C), 127.12 (2C), 125.00 (4C), 123.60 (2C), 123.33 (2C), 122.44 (1C, q, $J_{C\text{-}F}$ = 275.7 Hz, CF_3), 120.67 (1C, q, $J_{C\text{-}F}$ = 275.9 Hz, CF_3), 118.87, 117.38, 113.65 ppm. ^{19}F NMR (470 MHz, $CDCl_3$): δ = -60.79 (3F, s, CF_3), -68.03 (3F, s, CF_3) ppm. HRMS (ESI-TOF) calculated for $C_{35}H_{22}F_6N_4ONa$ [M + Na]$^+$: 651.1596, found: 651.1591.

***N*-(5,7-Bis(trifluoromethyl)-1,8-naphthyridin-2-yl)-5-(4-(diphenylamino)phenyl)thiophene-2-carboxamide (20)** was obtained as an orange crystalline solid in 51% yield (337 mg) using general procedure B from bromo-derivative **15** (485 mg, 1.03 mmol). ^{1}H NMR (500 MHz, $CDCl_3$): δ = 9.00 (1H, s, NH), 8.95 (1H, d, J = 9.3 Hz, naphthyridine-H), 8.60 (1H, d, J = 9.5 Hz, naphthyridine-H), 8.01 (1H, s, naphthyridine-H), 7.69 (1H, d, J = 4.0 Hz, thiophene-H), 7.49–7.52 (2H, m, Ar-H), 7.27–7.32 (5H, m, Ar-H, thiophene-H), 7.14–7.16 (4H, m, Ar-H), 7.07–7.11 (4H, m, Ar-H) ppm. ^{13}C{H} NMR (125 MHz, $CDCl_3$): δ = 160.41, 155.63, 154.78, 152.78, 151.16 (1C, q, $J_{C\text{-}F}$ = 36.4 Hz, C-CF_3), 149.13, 147.17 (2C), 138.04 (1C, q, $J_{C\text{-}F}$ = 33.2 Hz, C-CF_3), 135.89,134.66, 131.39, 129.63 (4C), 127.24 (2C), 126.24, 125.29 (4C), 123.98 (2C), 123.08, 122.67 (2C), 122.44 (1C, q, $J_{C\text{-}F}$ = 275.3 Hz, CF_3), 120.67 (1C, q, $J_{C\text{-}F}$ = 275.9 Hz, CF_3), 118.84, 117.33, 113.61 ppm. ^{19}F NMR (470 MHz, $CDCl_3$): δ = -60.83 (3F, s, CF_3), -68.08 (3F, s, CF_3) ppm. HRMS (ESI-TOF) calculated for $C_{33}H_{20}F_6N_4OSNa$ [M + Na]$^+$: 657.1160, found: 657.1164.

4.2.4 | General Procedure C: Synthesis of Boron Complexes 1–4

N, *N*-Diisopropylethylamine (1.57–1.99 mL, 9.00–11.43 mmol, 20 equiv) and $BF_3{\cdot}Et_2O$ (0.56–0.71 mL, 4.50–5.72 mmol, 10 equiv) were added to a solution of amide **17–20** (0.45–0.57 mmol, 1 equiv) in dry DCM (20 mL) under an argon atmosphere. The reaction mixture was stirred at room temperature for 24 h, then saturated aqueous $NaHCO_3$ (40 mL) was added. The mixture was extracted with DCM (3 × 20 mL). The collected organic layers were dried over anhydrous Na_2SO_4, filtered, and concentrated under reduced pressure. The crude product was purified by flash column chromatography (hexanes/DCM, 4:1 → 1:2, v/v).

4'-(1,1-Difluoro-7,9-dimethyl-1*H*-1λ^4,11λ^4-[1,3,5,2]oxadiazaborinino[3,4-*a*][1,8]naphthyridin-3-yl)-*N*,*N*-diphenyl-[1,1'-biphenyl]-4-amine (1) was obtained as an orange crystalline solid in 67% yield (214 mg) using general procedure C from amide **17** (292 mg, 0.56 mmol). ^{1}H NMR (500 MHz, $CDCl_3$): δ = 8.46–8.51 (3H, m, Ar-H, naphthyridine-H), 7.71 (2H, d, J = 8.4 Hz, Ar-H), 7.56 (2H, d, J = 8.4 Hz, Ar-H), 7.47 (1H, d, J = 9.0 Hz, naphthyridine-H), 7.29 (4H, dd, J = 8.4 Hz, J = 7.4 Hz, Ar-H), 7.26 (1H, s, naphthyridine-H), 7.16 (6H, m, Ar-H), 7.07 (2H, t, J = 7.4 Hz, Ar-H), 2.81 (3H, s, CH_3), 2.68 (3H, s, CH_3) ppm; ^{13}C{H} NMR (125 MHz, $CDCl_3$): δ = 167.69, 164.18, 158.28, 148.82, 148.22, 147.40 (2C), 145.75, 145.37, 139.19, 133.20, 130.72 (2C), 130.18, 129.36 (4C), 127.97 (2C), 126.30 (2C), 124.77 (4C), 123.98, 123.34 (2C), 123.28 (2C), 121.77, 118.71, 25.91, 18.15 ppm; ^{19}F NMR (470 MHz, $CDCl_3$): δ = -130.40 (2F, m, BF_2) ppm. HRMS (ESI-TOF) calculated for $C_{35}H_{27}BN_4OF_2Na$ [M + Na]$^+$: 591.2144, found: 591.2160.

4-(5-(1,1-Difluoro-7,9-dimethyl-1*H*-1λ^4,11λ^4-[1,3,5,2]oxadiazaborinino[3,4-*a*][1,8]naphthyridin-3-yl)thiophen-2-yl)-*N*,*N*-diphenylaniline (2) was obtained as an orange crystalline solid in 71% yield (234 mg) using general procedure C from amide **18** (301 mg, 0.57 mmol). ^{1}H NMR (500 MHz, $CDCl_3$): δ = 8.45 (1H, d, J = 9.0 Hz, naphthyridine-H), 8.08 (1H, d, J = 4.0 Hz, thiophene-H), 7.55 (2H, d, J = 8.8 Hz, Ar-H), 7.39 (1H, d, J = 9.0 Hz, naphthyridine-H), 7.28–7.32 (5H, m, thiophene-H, Ar-H), 7.24 (1H, d, J = 0.3 Hz, naphthyridine-H), 7.14–7.16 (4H, m, Ar-H), 7.07–7.10 (4H, m, Ar-H), 2.80 (3H, s, CH_3), 2.67 (3H, d, J = 0.6 Hz, CH_3) ppm; ^{13}C{H} NMR (125 MHz, $CDCl_3$): 163.79, 163.50, 157.90, 153.72, 148.73, 148.60, 146.84 (2C), 145.07, 138.69, 135.91, 133.66, 129.21 (4C), 126.85 (2C), 126.49, 124.85 (4C), 123.58, 123.49 (2C), 123.23, 122.37 (2C), 121.27, 118.20, 25.65, 17.92 ppm. ^{19}F NMR (470 MHz, $CDCl_3$): δ = -131.05 (2F, m, BF_2) ppm. HRMS (ESI-TOF) calculated for $C_{33}H_{26}BN_4OF_2S$ [M + H]$^+$: 575.1888, found: 575.1902.

4'-(1,1-Difluoro-7,9-bis(trifluoromethyl)-1*H*-1λ^4,11λ^4-[1,3,5,2]oxadiazaborinino[3,4-*a*][1,8]naphthyridin-3-yl)-*N*,*N*-diphenyl-[1,1'-biphenyl]-4-amine (3) was obtained as a dark red crystalline solid in 70% yield (212 mg) using general procedure C from amide **19** (283 mg, 0.45 mmol). ^{1}H NMR (500 MHz, $CDCl_3$): δ = 8.62 (1H, d, J = 9.0 Hz, naphthyridine-H), 8.50 (2H, d, J = 8.5 Hz, Ar-H), 8.11 (1H, s, naphthyridine-H), 7.71–7.76 (3H, m, Ar-H, naphthyridine-H), 7.56 (2H, d, J = 8.7 Hz, Ar-H), 7.29–7.31 (4H, m, Ar-H), 7.15–7.17 (6H, m, Ar-H), 7.07–7.10 (2H, m, Ar-H); ^{13}C{H} NMR (125 MHz, $CDCl_3$): δ = 170.75, 160.16, 150.70 (1C, q, $J_{C\text{-}F}$ = 37.6 Hz, C-CF_3), 148.98, 148.64, 147.26 (2C), 147.14, 137.91 (1C, q, $J_{C\text{-}F}$ = 33.9 Hz, C-CF_3), 137.50, 132.48, 131.54 (2C), 129.42 (4C), 129.12, 128.03 (2C), 128.00, 126.45 (2C), 124.96 (4C), 123.57 (2C), 122.96 (2C), 121.91 (1C, q, $J_{C\text{-}F}$ = 275.3 Hz, CF_3), 120.07 (1C, q, $J_{C\text{-}F}$ = 275.8 Hz, CF_3), 117.53, 114.99 ppm. ^{19}F NMR (470 MHz, $CDCl_3$): δ = -60.36 (3F, s, CF_3), -67.90 (3F, s, CF_3), -130.46 (2F, m, BF_2) ppm. HRMS (ESI-TOF) calculated for $C_{35}H_{21}BN_4OF_8Na$ [M + Na]$^+$: 699.1578, found: 699.1575.

4-(5-(1,1-Difluoro-7,9-bis(trifluoromethyl)-1*H*-1λ^4,11λ^4-[1,3,5,2]oxadiazaborinino[3,4-*a*][1,8]naphthyridin-3-yl)thiophen-2-yl)-*N*,*N*-diphenylaniline (4) was obtained as a black crystalline solid in 73% yield (252 mg) using general procedure C from amide **20** (320 mg, 0.50 mmol). ^{1}H NMR (500 MHz, $CDCl_3$): δ = 8.53 (1H, d, J = 8.1 Hz, naphthyridine-H), 8.17 (1H, d, J = 4.1 Hz, thiophene-H), 8.07 (1H, s, naphthyridine-H), 7.62 (1H, d, J = 9.4 Hz, naphthyridine-H), 7.56 (2H, d, J = 8.6 Hz, Ar-H), 7.30–7.35 (5H, m, Ar-H, thiophene-H), 7.14–7.18 (4H, m, Ar-H), 7.06–7.13 (4H, m, Ar-H) ppm; ^{13}C{H} NMR (125 MHz, $CDCl_3$): δ = 166.30, 159.94, 157.18, 150.66 (1C, q, $J_{C\text{-}F}$ = 33.7 Hz, C-CF_3), 149.60, 149.38, 147.02 (2C), 138.43, 137.91 (1C, q, $J_{C\text{-}F}$ = 37.6 Hz, C-CF_3), 137.12, 132.94, 129.69 (4C), 127.92, 127.44 (2C), 126.12, 125.49 (4C), 124.22 (2C), 124.12, 122.28 (2C), 122.10 (1C, q, $J_{C\text{-}F}$ = 275.6 Hz, CF_3), 120.26 (1C, q, $J_{C\text{-}F}$ = 275.8 Hz, CF_3), 117.45, 114.80 ppm. ^{19}F NMR (470 MHz, $CDCl_3$): δ = -60.39 (3F, s, CF_3), -67.93 (3F, s, CF_3), -131.49 (2F, m, BF_2) ppm. HRMS (ESI-TOF) calculated for $C_{33}H_{19}BN_4OF_8SNa$ [M + Na]$^+$: 705.1143, found: 705.1144.

Acknowledgements

This project has received funding from the Research Council of Lithuania (LMTLT), project QUANT, agreement No S-LU-24–8 (Ukrainian: M/52-2024, No 0124U002941). We gratefully acknowledge the Polish high-performance computing infrastructure PLGrid (HPC Centers: ACK Cyfronet AGH, WCSS) for providing computer facilities and support within the computational Grant Number. PLG/2025/018787. We are also sincerely grateful to Dr. Katarzyna Rybicka-Jasińska, Prof. Daniel T. Gryko, and Prof. Agnieszka Szumna (Institute of Organic Chemistry, Polish Academy of Sciences) for permission to use their instruments.

Open access funding enabled and organized by Projekt DEAL.

Conflicts of Interest

The authors declare no conflict of interest.

Data Availability Statement

CCDC 2523545, 2523589 and 2548250 contain the supplementary crystallographic data for this paper. These data can be obtained free of charge from The Cambridge Crystallographic Data Centre via www.ccdc.cam.ac.uk/data_request/cif.

References

1. D. Zhang, T. Huang, and L. Duan, "Emerging Self-Emissive Technologies for Flexible Displays," *Advanced Materials* 32 (2020): 1902391, https://doi.org/10.1002/adma.201902391.

2. D. Jiang, H. Sasabe, H. Arai, K. Nakao, K. Kumada, and J. Kido, "Extremely High Power Efficiency Solution-Processed Orange-Red TADF OLEDs via a Synergistic Strategy of Molecular and Device Engineering," *Advanced Optical Materials* 10 (2022): 2102774, https://doi.org/10.1002/adom.202102774.

3. X. Cai, Y. Pan, X. Song, et al., "Precisely Regulation of Peripheral Decoration of Multi-Resonance Molecules and Construction of Highly Efficient Solution-Processed Orange–Red OLEDs With External Quantum Efficiency Approaching 20%," *Advanced Optical Materials* 12 (2024): 2302811, https://doi.org/10.1002/adom.202302811.

4. K. R. Naveen, K. Prabhu CP, R. Braveenth, and J. H. Kwon, "Molecular Design Strategy for Orange Red Thermally Activated Delayed Fluorescence Emitters in Organic Light-Emitting Diodes (OLEDs)," *Chemistry–A European Journal* 28 (2022): 202103532, https://doi.org/10.1002/chem.202103532.

5. D. Karthik, Y. H. Jung, H. Lee, et al., "Acceptor–Donor–Acceptor-Type Orange–Red Thermally Activated Delayed Fluorescence Materials Realizing External Quantum Efficiency Over 30% With Low Efficiency Roll-Off," *Advanced Materials* 33 (2021): 2007724, https://doi.org/10.1002/adma.202007724.

6. A. C. Murali, P. Nayak, and K. Venkatasubbaiah, "Recent Advances in the Synthesis of Luminescent Tetra-Coordinated Boron Compounds," *Dalton Transactions* 51 (2022): 5751–5771, https://doi.org/10.1039/D2DT00160H.

7. H. Ye, D. H. Kim, X. Chen, et al., "Near-Infrared Electroluminescence and Low Threshold Amplified Spontaneous Emission Above 800 nm From a Thermally Activated Delayed Fluorescent Emitter," *Chemistry of Materials* 30 (2018): 6702–6710, https://doi.org/10.1021/acs.chemmater.8b02247.

8. D. Frath, J. Massue, G. Ulrich, and R. Ziessel, "Luminescent Materials: Locking π-Conjugated and Heterocyclic Ligands With Boron(III)," *Angewandte Chemie International Edition* 53 (2014): 2290–2310, https://doi.org/10.1002/anie.201305554.

9. L. J. Patalag, J. A. Ulrichs, P. G. Jones, and D. B. Werz, "Decorated BODIPY Fluorophores and Thiol-Reactive Fluorescence Probes by an Aldol Addition," *Organic Letters* 19 (2017): 2090–2093, https://doi.org/10.1021/acs.orglett.7b00693.

10. J. Zhang, N. Wang, X. Ji, Y. Tao, J. Wang, and W. Zhao, "BODIPY-Based Fluorescent Probes for Biothiols," *Chemistry—A European Journal* 26 (2020): 4172–4192, https://doi.org/10.1002/chem.201904470.

11. Z. Wang, T. Pan, Y. Tian, and J. Liao, "A Near-Infrared Probe for the Real-Time Detection of Lysosomal pH in Living Cells Under "Wash Free" Conditions," *Journal of Materials Chemistry B* 10 (2022): 7045–7051, https://doi.org/10.1039/D2TB01441F.

12. A. Hajda, M. Grelich-Mucha, P. Rybczyński, B. Osmiałowski, R. Zalesný, and J. Olesiak-Bańska, "BF 2 -Functionalized Benzothiazole Amyloid Markers: Effect of Donor Substituents on One- and Two-Photon Properties," *ACS Applied Bio Materials* 6 (2023): 5676–5684, https://doi.org/10.1021/acsabm.3c00815.

13. S. Li, J. Chen, Y. Wei, et al., "An Organic Laser Based on Thermally Activated Delayed Fluorescence With Aggregation-Induced Emission and Local Excited State Characteristics," *Angewandte Chemie International Edition* 61 (2022): 202209211, https://doi.org/10.1002/anie.202209211.

14. R. Aoki, R. Komatsu, K. Goushi, et al., "Realizing Near-Infrared Laser Dyes Through a Shift in Excited-State Absorption," *Advanced Optical Materials* 9 (2021): 2001947, https://doi.org/10.1002/adom.202001947.

15. R. Pytlarz, S. Kutsiy, A. Hotynchan, et al., "Benzochalcogenazolo-Based N, O -Coordinated Boron Difluoride Complexes as Gain Media for Organic Solid-State Lasers," *Journal of Materials Chemistry C* 13 (2025): 16478–16488, https://doi.org/10.1039/D5TC02236C.

16. M. Collot, T. K. Fam, P. Ashokkumar, et al., "Ultrabright and Fluorogenic Probes for Multicolor Imaging and Tracking of Lipid Droplets in Cells and Tissues," *Journal of the American Chemical Society* 140 (2018): 5401–5411, https://doi.org/10.1021/jacs.7b12817.

17. A. Albers, S. Kuberasivakumaran, Z. Fernández, et al., "Size-Controlled Self-Assembly for Bimodal In Vivo Imaging," *Angewandte Chemie International Edition* 64 (2025): 202500144, https://doi.org/10.1002/anie.202500144.

18. A. D'Aléo, M. H. Sazzad, D. H. Kim, et al., "Boron Difluoride Hemicurcuminoid as an Efficient Far Red to Near-Infrared Emitter: Toward OLEDs and Laser Dyes," *Chemical Communications* 53 (2017): 7003–7006, https://doi.org/10.1039/C7CC01786C.

19. J. Brodeur, L. Hu, A. Malinge, E. Eizner, W. G. Skene, and S. Kéna-Cohen, "Highly Efficient and Spectrally Narrow Near-Infrared Fluorescent OLEDs Using a TADF-Sensitized Cyanine Dye," *Advanced Optical Materials* 7 (2019): 1901144, https://doi.org/10.1002/adom.201901144.

20. P. Xue, X. Wang, W. Wang, et al., "Solution-Processable Chiral Boron Complexes for Circularly Polarized Red Thermally Activated Delayed Fluorescent Devices," *ACS Applied Materials & Interfaces* 13 (2021): 47826–47834, https://doi.org/10.1021/acsami.1c13564.

21. S. Kutsiy, D. Volyniuk, S. R. Sahoo, et al., "Sterically Tuned Ortho -Phenylene-Linked Donor–Acceptor Benzothiazole-Based Boron Difluoride Complexes as Thermally-Activated Delayed Fluorescence Emitters for Organic Light-Emitting Diodes," *ACS Applied Materials & Interfaces* 16 (2024): 60633–60647, https://doi.org/10.1021/acsami.4c12662.

22. Q. Qi, S. Huang, X. Liu, and I. Aprahamian, "1,2-BF 2 Shift and Photoisomerization Induced Multichromatic Response," *Journal of the American Chemical Society* 146 (2024): 6471–6475, https://doi.org/10.1021/jacs.4c00592.

23. M. Louis, R. Sethy, J. Kumar, et al., "Mechano-Responsive Circularly Polarized Luminescence of Organic Solid-State Chiral Emitters," *Chemical Science* 10 (2019): 843–847, https://doi.org/10.1039/C8SC04026E.

24. Y. V. Zatsikha, T. S. Blesener, A. J. King, et al., "Fully Conjugated Pyrene–BODIPY and Pyrene–BODIPY–Ferrocene Dyads and Triads: Synthesis, Characterization, and Selective Noncovalent Interactions With Nanocarbon Materials," *The Journal of Physical Chemistry B* 125 (2021): 360–371, https://doi.org/10.1021/acs.jpcb.0c10074.

25. M. A. Potopnyk, D. Volyniuk, R. Luboradzki, A. Lazauskas, and J. V. Grazulevicius, "Aggregation-Induced Emission-Active Carbazolyl-Modified Benzo[4,5]thiazolo[3,2- c]Oxadiazaborinines as Mechanochromic Fluorescent Materials," *European Journal of Organic Chemistry* 2021 (2021): 2772–2781, https://doi.org/10.1002/ejoc.202100239.

26. S. Kutsiy, O. Bezvikonnyi, A. Hotynchan, et al., "Donor–Acceptor Boron Difluoride Complexes for Bipolar Exciplex Emitters in Organic Light-Emitting Diodes," *ACS Applied Materials & Interfaces* 17 (2025): 60956–60968, https://doi.org/10.1021/acsami.5c17456.

27. M. A. Potopnyk, J. Mech-Piskorz, G. Angulo, et al., "Aggregation/Crystallization-Induced Emission in Naphthyridine-Based Carbazolyl-Modified Donor-Acceptor Boron Dyes Tunable by Fluorine Atoms," *Chemistry–A European Journal* 30 (2024): 202400004, https://doi.org/10.1002/chem.202400004.

28. E. V. Puttock, J. Haug, E. Zysman-Colman, and S. Bräse, "Hyperphosphorescent OLEDs: Harnessing the Power of MR-TADF Terminal Emitters," *Advanced Optical Materials* 13 (2025): 2500514, https://doi.org/10.1002/adom.202500514.

29. J. S. Ahadzadeh, S. Brebels, W. Maes, and W. Deferme, "Strategies for Advancing Near-Infrared Organic Light-Emitting Diodes: Innovations in Luminescent Materials, Device Architectures, Fabrication Methods, and Applications," *Advanced Functional Materials* 36 (2026): 2419599, https://doi.org/10.1002/adfm.202419599.

30. S. Li, X. Zhou, L. Xu, et al., "Beyond 800 nm: Recent Progress in High-Performance Near-Infrared Thermally Activated Delayed Fluorescence Based OLEDs," *Chemical Science* 17 (2026): 4863–4880, https://doi.org/10.1039/D5SC09087C.

31. D. K. A. P. Huu, S. Saseendran, R. Dhali, et al., "Thermally Activated Delayed Fluorescence: Polarity, Rigidity, and Disorder in Condensed Phases," *Journal of the American Chemical Society* 144, no. 33 (2022): 15211–15222, https://doi.org/10.1021/jacs.2c05537.

32. W. He, H. Huang, K.-N. Tong, et al., "Dual-Exciplex White OLEDs for Natural-Quality Lighting and Optical Data Transmission," *Advanced Materials* 38 (2025): 19228, https://doi.org/10.1002/adma.202519228.

33. V. Jankus, P. Data, D. Graves, et al., "Highly Efficient TADF OLEDs: How the Emitter–Host Interaction Controls Both the Excited State Species and Electrical Properties of the Devices to Achieve Near 100% Triplet Harvesting and High Efficiency," *Advanced Functional Materials* 24 (2014): 6178–6186, https://doi.org/10.1002/adfm.201400948.

34. K. Goushi, K. Yoshida, K. Sato, and C. Adachi, "Organic Light-Emitting Diodes Employing Efficient Reverse Intersystem Crossing for Triplet-to-Singlet State Conversion," *Nature Photonics* 6 (2012): 253–258, https://doi.org/10.1038/nphoton.2012.31.

35. H. Zhang, Z. Wang, L. Gao, B. Zhao, and W. Li, "Low Efficiency Roll-Off and High Color Stability Pure Fluorescent White Organic Light-Emitting Diode Based Exciplex Host," *RSC Advances* 8 (2018): 954–959, https://doi.org/10.1039/C7RA11325K.

36. J. Hua, L. Qi, Z. Cheng, et al., "High Efficiency and Low Roll-off White Phosphorescent Organic Light-Emitting Diodes by Employing Various

Acceptor Ratio in Exciplex-Forming Co-Host," *Dyes and Pigments* 235 (2025): 112621, https://doi.org/10.1016/j.dyepig.2024.112621.

37. W.-Y. Hung, G.-C. Fang, S.-W. Lin, et al., "The First Tandem, All-Exciplex-Based WOLED," *Scientific Reports* 4 (2014): 5161, https://doi.org/10.1038/srep05161.

38. M. Guzauskas, D. Volyniuk, A. Tomkeviciene, A. Pidluzhna, A. Lazauskasc, and J. V. Grazulevicius, "Dual Nature of Exciplexes: Exciplex-Forming Properties of Carbazole and Fluorene Hybrid Trimers," *Journal of Materials Chemistry C* 7 (2019): 25–32, https://doi.org/10.1039/C8TC04708A.

39. M. Zhang, D.-M. Sun, K. Wang, et al., "Dendritic Oligomers-Based Exciplex Emitters Realizing Solution-Processed Organic Light-Emitting Diodes With Nearly 30% External Quantum Efficiency," *Advanced Functional Materials* 35 (2025): 2414808, https://doi.org/10.1002/adfm.202414808.

40. D. Chen, K. Liu, L. Gan, et al., "Modulation of Exciton Generation in Organic Active Planar pn Heterojunction: Toward Low Driving Voltage and High-Efficiency OLEDs Employing Conventional and Thermally Activated Delayed Fluorescent Emitters," *Advanced Materials* 28 (2016): 6758–6765, https://doi.org/10.1002/adma.201600612.

41. Y. Yuan, Y. Hu, Y.-X. Zhang, et al., "Over 10% EQE Near-Infrared Electroluminescence Based on a Thermally Activated Delayed Fluorescence Emitter," *Advanced Functional Materials* 27 (2017): 1700986, https://doi.org/10.1002/adfm.201700986.

42. D.-H. Kim, A. D'Aléo, X.-K. Chen, et al., "High-Efficiency Electroluminescence and Amplified Spontaneous Emission From a Thermally Activated Delayed Fluorescent Near-Infrared Emitter," *Nature Photonics* 12 (2018): 98–104, https://doi.org/10.1038/s41566-017-0087-y.

43. X. Yang, S. Zhuang, X. Qiao, et al., "High Efficiency Blue Phosphorescent Organic Light-Emitting Diodes With a Multiple Quantum Well Structure for Reduced Efficiency Roll-off," *Optics Express* 20 (2012): 24411, https://doi.org/10.1364/OE.20.024411.

44. H. Zhu, Z. Xu, S. Zhao, et al., "Study on the Influences of Quantum Well Structure on the Performance of Organic Light Emitting Devices," *Displays* 32 (2011): 102–105, https://doi.org/10.1016/j.displa.2010.12.003.

45. L. Deva, P. Stakhira, V. Fitio, et al., "Organic Light-Emitting Devices with Quantum Well Structures Using Carbazole Derivative 4CZTPN-Ph as an the Emitting Material," *Ukrainian Journal of Physical Optics* 26, no. 1 (2025): 01009–01022, https://doi.org/10.3116/16091833/Ukr.J.Phys.Opt.2025.01009.

46. Y. Sun, W. Sun, W. Liu, X. Li, J. Yin, and L. Zhou, "Efficient Nondoped Pure Red/Near-Infrared TADF OLEDs by Designing and Adjusting Double Quantum Wells Structure," *ACS Applied Electronic Materials* 4, no. 7 (2022): 3615–3622, https://doi.org/10.1021/acsaelm.2c00531.

47. S. Wang, X. Yan, Z. Cheng, H. Zhang, Y. Liu, and Y. Wang, "Highly Efficient Near-Infrared Delayed Fluorescence Organic Light Emitting Diodes Using a Phenanthrene-Based Charge-Transfer Compound," *Angewandte Chemie International Edition* 54 (2015): 13068–13072, https://doi.org/10.1002/anie.201506687.

48. S. Wang, Z. Cheng, X. Song, et al., "Highly Efficient Long-Wavelength Thermally Activated Delayed Fluorescence OLEDs Based on Dicyanopyrazino Phenanthrene Derivatives," *ACS Applied Materials & Interfaces* 9 (2017): 9892–9901, https://doi.org/10.1021/acsami.6b14796.

49. A. K. Gupta, D. B. Cordes, J. De, et al., "Deep-red to NIR Solution-Processed OLEDs of Donor-Decorated Quinoxaline-Based TADF Aggregates," *Journal of Materials Chemistry C* 13 (2025): 6123–6135, https://doi.org/10.1039/D4TC05238B.

50. Agilent Technologies, CrysAlisPro, Version 1171.38.46.

51. G. M. Sheldrick, "SHELXT—Integrated Space-Group and Crystal-Structure Determination," *Acta Crystallographica Section A Foundations and Advances* 71 (2015): 3–8, https://doi.org/10.1107/S2053273314026370.

52. L. J. Farrugia, "WinGX Suite for Small-Molecule Single-Crystal Crystallography," *Journal of Applied Crystallography* 32 (1999): 837–838, https://doi.org/10.1107/S0021889899006020.

53. M. J. Frisch, G. W. Trucks, H. B. Schlegel, et al., *Gaussian* 16 (2016).

54. R. Dennington, T. A. Keith, and J. M. Millam, *GaussView, Version 6* (Semichem Inc, 2016).

Supporting Information

Additional supporting information can be found online in the Supporting Information section.

Supporting File 1: adom71354-sup-0001-SuppMat.pdf.

Supporting File 2: adom71354-sup-0002-Data.zip.